



저작자표시 2.0 대한민국

이용자는 아래의 조건을 따르는 경우에 한하여 자유롭게

- 이 저작물을 복제, 배포, 전송, 전시, 공연 및 방송할 수 있습니다.
- 이차적 저작물을 작성할 수 있습니다.
- 이 저작물을 영리 목적으로 이용할 수 있습니다.

다음과 같은 조건을 따라야 합니다:



저작자표시. 귀하는 원저작자를 표시하여야 합니다.

- 귀하는, 이 저작물의 재이용이나 배포의 경우, 이 저작물에 적용된 이용허락조건을 명확하게 나타내어야 합니다.
- 저작권자로부터 별도의 허가를 받으면 이러한 조건들은 적용되지 않습니다.

저작권법에 따른 이용자의 권리는 위의 내용에 의하여 영향을 받지 않습니다.

이것은 [이용허락규약\(Legal Code\)](#)을 이해하기 쉽게 요약한 것입니다.

[Disclaimer](#) 

이학석사학위논문

**Studies on Electrical and Structural Properties in
Oxygen Level Controlled BaSnO_{3-δ} Single Crystals**

산소 조성 조절에 따른 BaSnO_{3-δ} 단결정의
전기적 및 구조적 특성에 관한 연구

2014년 8월

서울대학교 대학원

물리천문학부

손 이 곤

**Studies on Electrical and Structural Properties in
Oxygen Level Controlled BaSnO_{3-δ} Single Crystals**

산소 조성 조절에 따른 BaSnO_{3-δ} 단결정의
전기적 및 구조적 특성에 관한 연구

지도 교수 김 기 훈

이 논문을 이학석사 학위논문으로 제출함

2014 년 8 월

서울대학교 대학원
물리천문학부
손 이 곤

손이곤의 이학석사 학위논문을 인준함

2014 년 6 월

위 원 장 _____ 유 재 준  (인)
부위원장 _____ 김 기 훈  (인)
위 원 _____ 차 국 린  (인)

Abstract

Transparent conducting oxides are gaining more interest because of its importance in display-related applications, photovoltaic, energy efficient windows and so on. Indium tin oxide, fluorine doped tin oxide and aluminium doped zinc oxides are the most widely used compounds in this field. However, they have drawbacks as well, such as high cost and oxygen instability issues. Our group previously succeeded in growing the single crystal of a possible replacement, BaSnO₃. The physical properties of perovskite structured barium stannate single crystals, BaSnO₃, (Ba,La)SnO₃, and Ba(Sn,Sb)O₃ were studied thoroughly. Especially, (Ba,La)SnO₃ has exhibited high mobility, 320 cm²V⁻¹S⁻¹, while maintaining its transparency. Also, there were efforts to grow (Ba,La)SnO₃ film with high mobility, but due to the lattice mismatch between (Ba,La)SnO₃ and the substrate, the mobility remained low, 70 cm²V⁻¹s⁻¹. Thus, undoped BaSnO₃ comes in fore as a lattice-matched substrate. However, previous data show that undoped BaSnO₃ has a carrier concentration of ~10¹⁸ cm⁻³ by the presence of oxygen vacancy.

In this thesis, we present that we successfully reduced oxygen vacancy in undoped BaSnO₃ crystals by adding an oxidizer during flux growth. The crystals are confirmed to be an identical cubic perovskite with a lattice parameter of $a=b=c=4.117 \text{ \AA}$. The reduction of oxygen vacancy led to a metal-insulator transition where the resistivity changed drastically from ~10⁻³ Ω·cm to ~10¹¹ Ω·cm at room temperature. The crystals with low resistivity were blue in color while the crystals with high resistivity were yellow. By optical spectroscopy ranging from mid-IR to UV, we observed that crystals grown with an oxidizer have significantly lower free carrier absorption. Moreover, through Raman spectroscopy, we noticed that the oxygen vacant

BaSnO_{3-δ} crystals show first-order Raman scattering which means that it is locally distorted even though the x-ray diffraction pattern shows a cubic perovskite structure. This may indicate that the presence of carrier in BaSnO_{3-δ} single crystal is closely related to local structure distortion. Through polarized Raman spectroscopy, we attempted to assign the observed first order Raman peaks. Additionally, we have investigated the external effects, such as polishing and forming gas annealing, on the structure of BaSnO_{3-δ} single crystals through Raman spectroscopy. In all, this dissertation focuses on the physical properties of BaSnO_{3-δ} single crystals while modifying the oxygen vacancy level by the use of an oxidizer.

Keywords: Transparent conducting oxides, BaSnO₃, cubic perovskite, Raman spectroscopy

Student Number: 2012-20366

Contents

| | |
|---|------------|
| Abstract | i |
| Contents | iii |
| List of Figures | v |
| List of Tables | vii |
| 1 Introduction | 1 |
| 2 Fundamentals | 5 |
| 2.1 Crystal structure and measurement | 5 |
| 2.1.1 Periodic structure and reciprocal space | 5 |
| 2.1.2 Bragg condition and X-ray diffraction | 7 |
| 2.2 Electrical transport properties | 10 |
| 2.3 Optical properties | 13 |
| 2.4 Raman spectroscopy..... | 17 |
| 2.4.1 General..... | 17 |
| 2.4.2 Polarized Raman spectroscopy..... | 21 |
| 2.4.3 Raman scattering intensity..... | 26 |
| 3 Experimental Details | 28 |
| 3.1 Single crystal growth..... | 28 |
| 3.2 Structure analysis | 30 |
| 3.3 Electrical transport | 30 |
| 3.4 Optical transmission..... | 31 |
| 3.5 Raman spectroscopy..... | 32 |
| 4 Results and Discussions | 33 |
| 4.1 Structure analysis | 33 |
| 4.1.1 X-ray diffraction..... | 33 |

| | | |
|----------|---|-----------|
| 4.1.2 | X-ray microdiffraction..... | 35 |
| 4.2 | Electrical transport | 37 |
| 4.2.1 | Temperature dependent resistivity..... | 37 |
| 4.3 | Optical transmission..... | 45 |
| 4.4 | Raman spectroscopy..... | 50 |
| 4.4.1 | BaSnO _{3-δ} Single crystals..... | 50 |
| 4.4.2 | External effect on crystal structure..... | 57 |
| 4.4.3 | Doped BaSnO ₃ single crystals..... | 62 |
| 5 | Conclusion | 64 |
| | Reference..... | 66 |
| | 국문 초록 | 68 |

List of Figures

| | |
|--|----|
| Figure 1-1 Carrier concentration verses mobility for transparent conducting oxides | 2 |
| Figure 1-2 Lattice constants of commercial substrates. | 3 |
| Figure 2-1 X-ray diffraction | 7 |
| Figure 2- θ - 2θ scan in reciprocal space..... | 8 |
| Figure 2-3 Laue diffraction in 90 degree scattering geometry. | 9 |
| Figure 2-4 Hall measurement. | 12 |
| Figure 2-5 Polarized Raman spectroscopy..... | 23 |
| Figure 3-1 Photos of BaSnO ₃ single crystals grown by flux growth | 29 |
| Figure 4-1 X-ray diffraction results..... | 34 |
| Figure 4-2 X-ray microdiffraction results | 36 |
| Figure 4-3 Temperature verses resistivity results in BaSnO ₃ single crystals . | 38 |
| Figure 4-4 Arrhenius plot and activation energy in BaSnO ₃ single crystals. . | 41 |
| Figure 4-5 Hall measurement results of low resistivity BaSnO ₃ single crystals (x=0-1)..... | 43 |
| Figure 4-6 Optical transmittance (near-IR to UV). | 46 |
| Figure 4-7 Optical transmittance and optical band gap..... | 48 |
| Figure 4-8 Depolarized Raman spectroscopy on BaSnO ₃ single crystals..... | 51 |
| Figure 4-9 Space group for perovksites under phase transitions..... | 52 |
| Figure 4-10 Polarized Raman spectroscopy results on BaSnO ₃ single crystals. | 55 |
| Figure 4-11 Raman spectroscopy on BaSnO ₃ single crystal (x=2) and polycrystal. | 56 |

Figure 4-12 Polishing and O₂ annealing effect in BaSnO₃ single crystal ($x=0$)
..... 58

Figure 4-13 Forming gas (H₂/Ar) annealing effect on BaSnO₃ single crystal
($x=2$) 61

Figure 4-14 Raman spectroscopy on doped BaSnO₃ single crystals..... 63

List of Tables

| | |
|--|----|
| Table 2-1 Spectral regions and their physical origin..... | 18 |
| Table 2-2 Mulliken Symbol notation and definition..... | 22 |
| Table 2-3 Crystal information of perovskites..... | 25 |
| Table 2-4 IR and Raman active modes in a perovskite..... | 25 |
| Table 4-1 Raman active modes under polarized Raman spectroscopy..... | 53 |

Chapter 1

Introduction

Previous studies had a limitation of understanding the intrinsic properties of BaSnO₃ because of the difficulties in growing large size crystals. However, Kim *et al.* from our research group have succeeded in growing BaSnO₃ single crystals by flux method [1]. The single crystals allowed our research group to investigate various intrinsic physical properties of BaSnO₃. The single crystals were highly transparent when they were thinned down to nearly 100 μm in thickness. From the optical transmission measurements, the optical band gap was extracted to be 3.1 eV. Meanwhile, our collaborators did band calculation which showed a dispersive conduction band. Therefore, we attempted to give electron carriers to the system by either doping the Ba site by La or doping the Sn site by Sb. The results were successful. Highly conductive single crystals were grown. The conductivity for (Ba,La)SnO₃ and Ba(Sn,Sb)O₃ were $\sim 10^4 \Omega^{-1}\text{cm}^{-1}$ and $\sim 10^3 \Omega^{-1}\text{cm}^{-1}$, respectively. Especially, (Ba,La)SnO₃ had a high mobility of $\sim 300 \text{cm}^2\text{V}^{-1}\text{s}^{-1}$ in room temperature [2, 3]. Comparing to other transparent conducting oxides with the same carrier concentration, BaSnO₃ has a higher mobility as shown in Figure 1-1 [4]. The wide optical gap and the high electron mobility along with the stability under different atmosphere made BaSnO₃ an interesting compound to investigate and to make practical use out of it [1].

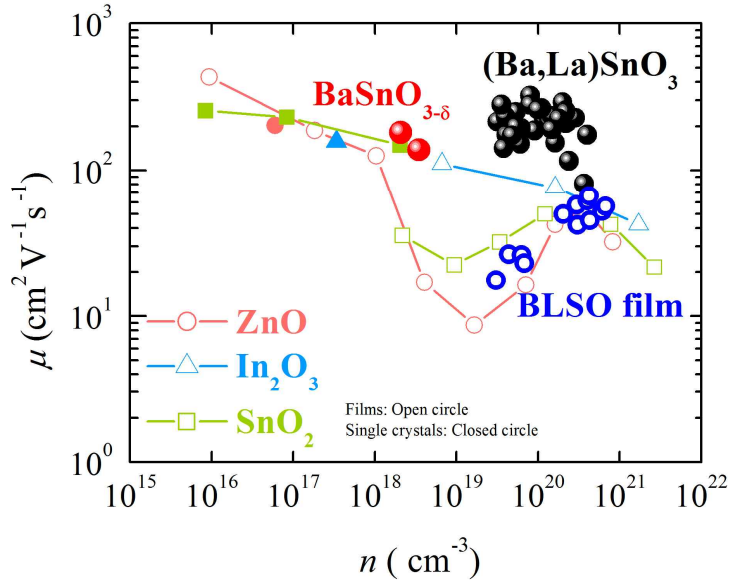


Figure 1-1 Carrier concentration and mobility values of typical transparent conducting oxides compared with BaSnO₃

Along with the studies in BaSnO₃ and (Ba,L)SnO₃ single crystals, there were efforts to grow epitaxial films. However, the mobility was disappointingly low compared to the single crystals. The mobility of (Ba,L)SnO₃ film grown on MgO substrate was 0.1–1 cm²V⁻¹s⁻¹ [5], (Ba, La)SnO₃ film grown on SrTiO₃ substrate were 70 cm²V⁻¹s⁻¹ [6] and 14.3 cm²V⁻¹s⁻¹ [7] which the highest value is still more than a factor three less than the mobility of single crystals. The reason for the lowering of mobility in films is thought to be the existence of thread dislocation in the (Ba,L)SnO₃ films. Through TEM images, it was confirmed that there were more thread dislocations in the case of lower mobility. Therefore, the importance of reducing thread dislocations in the film has become an important factor to increase the electron carrier mobility in BaSnO₃ films. The thread dislocations are thought to be present due to the lattice mismatch between the SrTiO₃ substrate (3.9 Å) and the (Ba,L)SnO₃ film (4.1 Å) [6]. The next step to

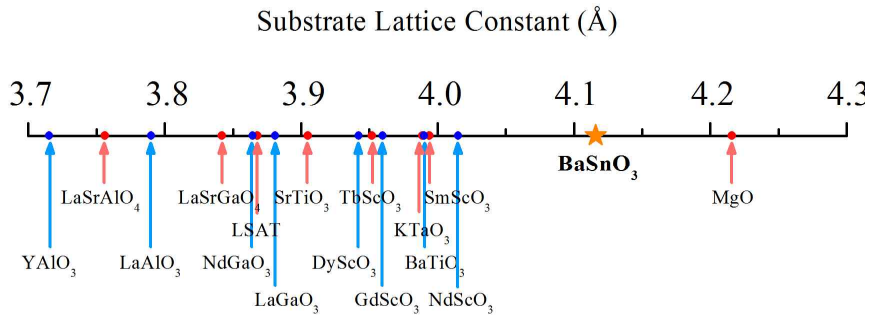


Figure 1-2 Comparison of the lattice constants between commercially available substrates and BaSnO₃ single crystal.

realize high mobility (Ba,La)SnO₃ film would be to use a substrate that has comparable lattice constants to the film. However, the lattice constants of commercially available substrates differ from that of BaSnO₃ greatly (Figure 1-2). Therefore, it is difficult to find a substrate that has the possibility to reduce the thread dislocation.

However, there is still a good substrate that has a well-matched lattice constant with (Ba,La)SnO₃. That is the undoped BaSnO₃ single crystal. There is no doubt that the undoped BaSnO₃ single crystal has nearly the same lattice constant. But there are several hurdles to overcome to use BaSnO₃ as a substrate. First of all, the grown single crystals are small in size, $\sim 2 \times 2 \times 1$ cm³. A larger substrate is preferable to measure physical properties and also in the point of application, it allows more devices to be fabricated on one substrate. Another issue is the fact that the undoped crystals grown under copper flux has oxygen vacancies. The electron carrier concentration due to oxygen vacancy was $\sim 2.0 - 3.0 \times 10^{18}$ cm²V⁻¹s⁻¹ [3]. The existence of the carriers is unfavorable when we use undoped single crystals as a substrate because it makes it difficult to measure the intrinsic electrical properties from the film on top. Therefore, it became an issue to realize truly insulating undoped BaSnO₃

single crystals to expand the horizon in the research of BaSnO₃ based films and also for practical device application.

Here in this dissertation, a growth method which our research group came up with to realize an undoped BaSnO₃ single crystal without oxygen vacancy will be introduced. Afterwards, the difference between the oxygen vacant BaSnO_{3-δ} and the oxygen rich BaSnO₃ single crystals are thoroughly investigated. The structural, electrical and optical properties were measured in order to understand the detailed physical properties in the two cases.

The remainder of this paper is organized as followed. First, the fundamental physics related to this study will be explained briefly. This will include the basics of x-ray diffraction, electrical resistivity, Hall measurement, optical transmission measurements, and Raman spectroscopy. Afterwards, the experimental details are described followed by the results. A brief conclusion will be given lastly.

Chapter 2

Fundamentals

2.1 Crystal structure and measurement

2.1.1 Periodic structure and reciprocal space

There are four states of matter we encounter in everyday life: solid, liquid, gas and plasma. And among them solid matter is the one we start our understanding in condensed matter physics. The first topic we learn in solid state physics is the periodicity in crystal structures. Probably this is because of the fact that it is a much easier case to understand the physical properties of collective atoms which are in a certain order than the case of them being randomly distributed. The amazing periodicity gives rise to all the physical properties that a solid has, such as electrical, thermal and optical properties. Therefore, knowing the atomic positions in a crystal becomes the first step of understanding the solid matter.

In a crystal, a group of atoms that repeats under translation fills up the whole space without an empty space. Here, the repeating group of atoms represents the unit cell of the crystal and we can define a discrete point that indicates the whole unit cell; this is called a lattice point and the lattice itself is called the Bravais lattice. The lattice points make an infinite array, and from the perspective of each lattice point, the lattice looks exactly the same. In another expression, we can define the position of a lattice point by three primitive vectors, $\vec{R} = n_1 \vec{a}_1 + n_2 \vec{a}_2 + n_3 \vec{a}_3$. However, each unit cell may have an additional symmetry within it and when we consider one lattice point and apply a certain symmetry operation on it, the lattice point we are considering

will remain the same. Such a symmetry operation on a lattice point gives 32 point groups. Considering the Bravais lattice and the 32 point groups all together, there are 73 space groups. There are two more operations, screw axis and glide plane operation, which gives 157 space groups. In total, there are 230 space groups that are possible.

A full description of each space group can be found in the *International Tables for Crystallography: Volume A. Space-Group Symmetry* [8]. The nomenclature for space groups are explained, and for each space group, the symmetry operation, Wyckoff positions, reflections and much more are summarized. Among them, the Wyckoff position is the representation of a group of positions in a unit cell which are identical through a certain symmetry operation. Each atom in a unit cell has its own Wyckoff position and it is often required to know it to analyze the data acquired from x-ray diffraction, IR spectroscopy and Raman spectroscopy of the crystal.

As mentioned, the periodicity of the structure gives rise to the physical properties of the crystal. However, more than the real lattice itself, a concept called reciprocal lattice is useful. When a plane wave $e^{i\vec{k}\cdot\vec{r}}$ has a periodicity exactly the same to the Bravais lattice, the wave vector \vec{K} also constitutes a set of lattice points, $\vec{K} = k_1\vec{b}_1 + k_2\vec{b}_2 + k_3\vec{b}_3$. \vec{b}_i are the primitive vectors which must satisfy

$$\vec{b}_i \cdot \vec{a}_j = 2\pi\delta_{ij} \quad (2-1)$$

and according to this relation \vec{b}_i is known to be as below.

$$\vec{b}_i = 2\pi \frac{\vec{a}_j \times \vec{a}_k}{|\vec{a}_1 \cdot \vec{a}_2 \times \vec{a}_3|} \quad (2-2)$$

This is the reciprocal lattice. This is useful since x-ray diffraction depends on

the distance between the planes of atoms. Also, the wave nature that electrons have makes it important to know the periodicity in reciprocal space to understand the electronic properties.

2.1.2 Bragg condition and X-ray diffraction

In 1913, W. L. Bragg and W. H. Bragg proposed that when an incident x-ray with specific wavelength is radiated upon a crystalline sample, intense peaks appeared at certain angles. They called this Bragg peaks and they suggested a model to explain this phenomena. Bragg accounted a plane of ions in the crystal to reflect the x-ray. The planes are apart by a distance d and each plane reflects the incident x-ray. An incident x-ray with wavelength λ is radiated upon the sample in an incident angle θ , an intense Bragg peaks appear according to the Bragg's condition which is as the following:

$$2d \sin \theta = n\lambda \quad (2-3)$$

Here n is the order of reflection.

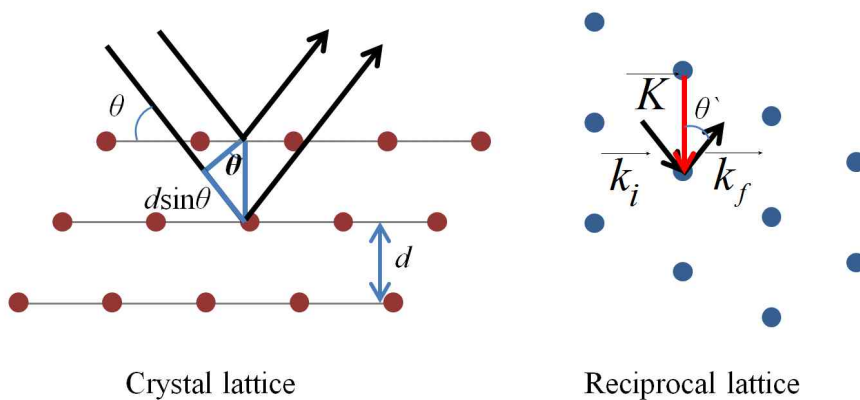


Figure 2-1 X-ray diffraction depicted in crystal lattice and reciprocal lattice. Note that $\theta' = 90 - \theta$.

As we have seen, the x-ray diffraction pattern actually directly gives the information of the reciprocal lattice. Since the real space lattice is correlated to the reciprocal lattice by equation 2-1 and 2-2, we can inversely know the real space by looking in to the x-ray diffraction pattern. Ever since the discovery of Bragg's condition, x-ray diffraction has become the most popular way to study the structure of crystalline samples. Various methods are present for different purposes. Among many, powder and single crystal x-ray diffraction and Laue method is briefly explained here.

The x-ray diffractometer consist a monochromatic x-ray source, detector and a sample stage. There are many different scan modes but the most commonly carried scan is the θ - 2θ scan. As illustrated in Figure 2-2, the x-ray source moves θ in respect to the sample surface while the detector moves 2θ in respect to the incident radiation direction. As θ is scanned for a given range, the effective scan in the reciprocal lattice is as the red arrows, in the normal direction to the sample surface. For the case of single crystals, the reciprocal space would be a set of discrete lattice points as the dark blue dots. Hence, only when the crystal is well aligned in respect to the reciprocal

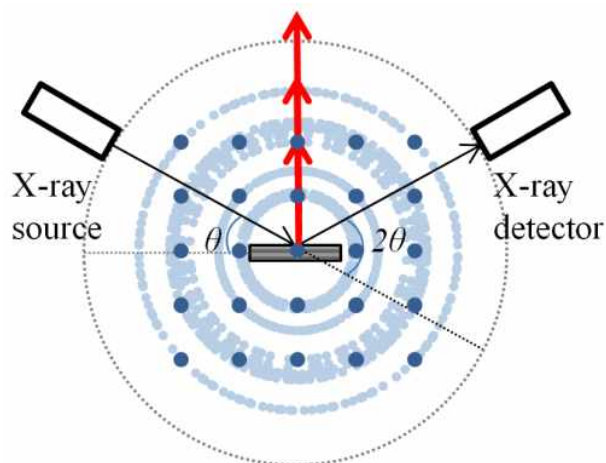


Figure 2-2 Schematic of θ - 2θ in reciprocal space.

lattices, the Bragg peaks corresponding to the normal planes will be observed. On the other hand, in the case of poly crystalline samples, the crystalline domains are randomly oriented resulting in a reciprocal space with the lattice points rotated as the light blue rings. Therefore all the possible Bragg peaks are observed.

Another useful tool to study crystals is the Laue diffractometer which is especially helpful to find the orientation of a crystal. Unlike the regular x-ray diffraction method, the Laue method uses a white beam (continuous wavelength) x-ray source and a two-dimensional detector. Thus, in the reciprocal space, the magnitude of the incident beam has a range of values depending on the source. Also, several Bragg peaks are detected at a single measurement due to the two-dimensional detector. Figure 2-3 shows the case of a Laue diffraction in 90° scattering. Since the x-ray source has a range of wavelengths, all the Bragg peaks (dark blue dots) between the two spheres with a radius of $\vec{k}_{i,\min}$ and $\vec{k}_{i,\max}$ are observable. Additionally, depending on the x-ray detector size, the observable Bragg peaks are restricted to the ones in the lightly shadowed area.

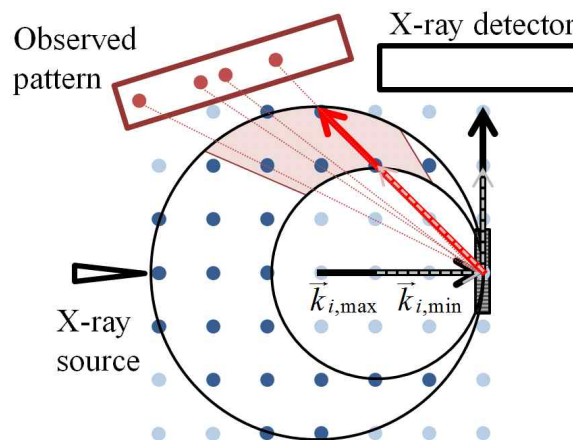


Figure 2-3 Schematic of Laue diffraction in 90 degree scattering in reciprocal space.

Depending on the purpose, a particular measurement is chosen. In this study, BaSnO₃ will be studied by both methods. The regular x-ray diffraction by the θ - 2θ scan will be done on the grinded powder to extract the lattice constants. Meanwhile, the Laue method is used to check the single crystal structure between the oxygen deficient and sufficient crystals.

2.2 Electrical transport properties

The electrical property of a material gives a myriad of information. The term *electrical property* is a very broad concept; however, among them, the most basic property is the electrical transport property. A brief summary of the electron transport by the classical Drude model will be given. Afterwards, Hall effect, which is a convenient way to measure the carrier concentration and mobility, will be introduced.

Electrical transport in metals is explained by the Drude model where the electrons are considered as if they are dilute neutral gas. Each electron is approximated to be free electrons between collisions. In other words, there are no additional field other than the one applied. Therefore, all the fields due to ions and electrons are neglected. Meanwhile, all the interactions with the moving electron such as electron-electron interaction, electron-phonon interaction, and impurity scattering are all together modeled to be an identical scattering source with an average collision time τ . The general law starts from the equation of motion.

$$m \frac{d\vec{v}}{dt} = \hbar \frac{d\vec{k}}{dt} = -e(\vec{E} + \vec{v} \times \vec{B}) \quad (2-4)$$

When we consider the situation with $\vec{B} = 0$, from the equation of motion we find that $\delta\vec{k} = -et\vec{E}/\hbar$. However, the momentum shift does not increase without a limit because the electric field effectively acts upon the electron for

only time t . Also, from the left side of equation 2-4, we find that $\vec{v} = \hbar \delta \vec{k} / m$. When we substitute the values to the equation for the current density \vec{j} while we consider the case of the average of time t which is the collision time τ , the current density is expressed as below:

$$\vec{j} = nq\vec{v}_{avg} = ne^2\tau\vec{E} / m. \quad (2-5)$$

Here n is the carrier concentration. Ohm's law states $\vec{j} = \sigma\vec{E}$ where σ is the conductivity. Therefore, we find the following relationship.

$$\sigma = \frac{ne^2\tau}{m} = ne\mu \quad (2-6)$$

The mobility (μ) is defined to express how the electron responds to the applied field: $\vec{v}_{avg} = \mu\vec{E}$.

Among the quantities mentioned above, the conductivity can be measured directly. However, to extract the carrier concentration and mobility, Hall effect measurements are required. The sample under investigation is prepared as Figure 2-4 where current source leads and voltage measurement leads are illustrated. The magnetic field is applied in the normal direction in respect to the sample surface. The magnetic field term in equation 2-4 is no longer zero. Also, a frictional damping term must be introduced to the equation of motion as below.

$$m\left(\frac{d}{dt} + \frac{1}{\tau}\right)\vec{v} = -e(\vec{E} + \vec{v} \times \vec{B}) \quad (2-7)$$

Due to the magnetic field, the carriers will accumulate on one side of the sample until equilibrium is reached. In the case of static state, the accumulated carriers will make an electric field which will prevent more carriers to pile up.

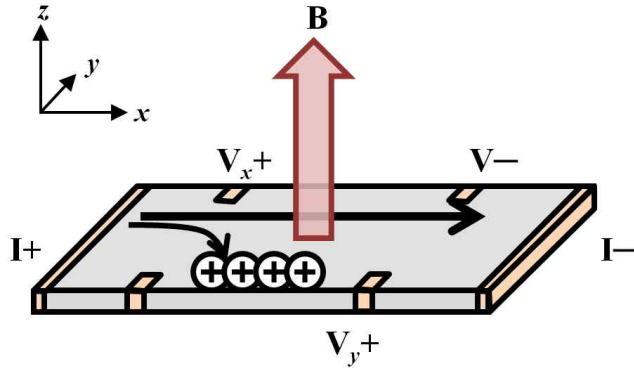


Figure 2-4 Hall measurement geometry.

Therefore, v_y is zero in static state. Substituting the conditions for static state, $v_y=0$ and $dv_x/dt=0$, and the relation $\vec{j} = -nev$, equation 2-7 becomes as the following.

$$E_y = -\frac{j_x}{ne} B_z \quad (2-8)$$

Therefore, by measuring the voltage induced between V_- and V_{y+} under the applied magnetic field B , the carrier concentration can be known. From equation 2-6, the mobility can be extracted too. More rigorous derivation can be found in reference 9.

2.3 Optical properties

To understand the physical properties, there are many different methods. Among the many, optical measurement is a method which is not destructive while giving a great range of information of the sample. Here, we briefly talk on the background knowledge that has been applied to investigate the BaSnO_{3.8} single crystals. First, a description on free carrier absorption in semiconductors will be given. Next, the relation between absorption coefficient and direct and indirect band gap will be briefly illustrated.

First, we start from explaining the motion of a bound electron in a material by a bound oscillator model. When we consider the free electrons which are not bound, we take the spring constant of the oscillator which results in a natural resonant frequency $\omega_0=0$. The Drude-Lorentz model considers the combination of the Drude model which models a free electron and the Lorentz model which considers the electron as a dipole oscillator. The equation of motion for the free electron under an oscillating electric field $E(t)=E_0e^{-i\omega t}$ becomes:

$$m_0 \frac{d^2x}{dt^2} + m_0\gamma \frac{dx}{dt} = -eE_0e^{-i\omega t}, \quad (2-9)$$

where the electron with a mass m_0 has a displacement of x with a damping rate γ . The electron will oscillate with the same frequency as the electric field, thus, $x=x_0e^{-i\omega t}$. Substituting this in to the equation of motion gives,

$$x = \frac{eE}{m_0(\omega^2 + i\gamma\omega)} \quad (2-10)$$

When there are N electrons per unit volume, the polarization becomes $P=-Nex$. Substituting the derived polarization into the definition of the electric displacement D , it becomes as the following.

$$\begin{aligned}
D &= \varepsilon_r \varepsilon_0 E \\
&= \varepsilon_0 E + P \\
&= \varepsilon_0 E - \frac{Ne^2 E}{m_0(\omega^2 + i\gamma\omega)} \\
&= \left(1 - \frac{Ne^2}{m_0 \varepsilon_0} \frac{1}{(\omega^2 + i\gamma\omega)}\right) \varepsilon_0 E
\end{aligned} \tag{2-11}$$

Here, we simplify $\varepsilon_r(\omega)$ by introducing plasma frequency ω_p as below.

$$\varepsilon_r(\omega) = 1 - \frac{\omega_p^2}{(\omega^2 + i\gamma\omega)}, \quad \omega_p = \left(\frac{Ne^2}{\varepsilon_0 m_0}\right)^{1/2} \tag{2-12}$$

Now we jump to the doped semiconductor case. Doped semiconductors have carriers due to the introduction of either a donor or an acceptor. The electron carriers will be moving in the conduction band while the hole carriers move in the valence band. When we consider the effective mass m^* of the carriers, the equations derived previously can be easily modified by replacing the electron mass to the effective mass. Also, the polarizability of the bound electrons before the dopants are added must be considered because the relative permittivity is high in semiconductors and because the contribution of free electrons are relatively low in the frequency range we are interested. The modified electric displacement becomes

$$D = \varepsilon_0 E + P_{\text{bound electrons}} + P_{\text{free electrons}} \tag{2-13}$$

Resulting from substitution and simplification, the resulting dielectric constant and plasma frequency is given by:

$$\varepsilon_r(\omega) = \varepsilon_{opt} \left(1 - \frac{\omega_p^2}{(\omega^2 + i\gamma\omega)}\right), \quad \omega_p^2 = \frac{Ne^2}{\varepsilon_{opt} \varepsilon_0 m^*} \tag{2-14}$$

We split the dielectric constant into its real and imaginary parts and substitute

the scattering rate τ^{-1} in place of γ .

$$\begin{aligned}\varepsilon_1 &= \varepsilon_{opt} \left(1 - \frac{\omega_p^2 \tau^2}{1 + \omega^2 \tau^2} \right) \\ \varepsilon_2 &= \frac{\varepsilon_{opt} \omega_p^2 \tau}{\omega(1 + \omega^2 \tau^2)}\end{aligned}\quad (2-15)$$

In a typical semiconductor, the scattering time is $\tau \sim 10^{-13}$ s which is also the same order in the case of (Ba,La)SnO₃. Therefore, at the frequencies in near-IR, an approximation $\omega\tau \gg 1$ is applicable. Also, this region of frequency is generally higher than the plasma frequency, $\omega \gg \omega_p$. Thus, we can assume $\varepsilon_1 \sim \varepsilon_{opt}$ and $\varepsilon_1 \gg \varepsilon_2$. Under these approximations, the real and imaginary part of the complex refractive index becomes $n = (\varepsilon_{opt})^{1/2}$ and $\kappa = \varepsilon_2 / 2n$. Therefore, the absorption coefficient results in below.

$$\alpha_{\text{free carrier}} = \frac{2\kappa\omega}{c} = \frac{2\omega}{c} \frac{\varepsilon_{opt} \omega_p^2 \tau}{2n\omega^3 \tau^2} = \frac{\varepsilon_{opt} \omega_p^2}{nc\omega^2 \tau} = \frac{Ne^2}{m^* \varepsilon_0 nc \tau} \frac{1}{\omega^2} \quad (2-16)$$

The final result shows that absorption occurs due to the free carriers, which is proportional to the carrier concentration and ω^{-2} .

While the free carrier absorption is observed at the near-IR region, the absorption due to interband transition can be observed at higher frequency region. An interband transition is the transition of an electron at a lower energy band to a higher energy band by absorbing a photon while satisfying the selection rule. In most cases, this occurs in semiconductors or in insulators where the valence band is filled and the conduction band is empty.

The band gap under consideration can be largely divided in to two, direct band gap and indirect band gap, depending on whether the position of valence band maximum and conduction band minimum are equal in the Brillouin zone. The direct band gap is the case where the valence band

maximum and the conduction band minimum are identically at the zone center, $k=0$. Meanwhile, for the indirect band gap case, the valence band maximum and the conduction band minimum are different. In this case for a photon to excite an electron in the valence band to the conduction band requires a momentum change in the electron. Since the momentum of a photon is nearly zero, a photon alone cannot produce a transition in an indirect band gap. Here, the phonon comes in role to allow the transition.

By analyzing the absorption coefficient verses frequency data, it is possible to find out the direct or indirect band gap. The derivation is too lengthy, thus we leave the derivation to reference 10 and note only the results.

$$\text{Direct interband transitions: } \alpha^2 \propto \hbar\omega - E_g$$

$$\text{Indirect inter band transitions: } \alpha^{1/2} \propto \hbar\omega - E_g \pm \hbar\omega_q \quad (2-17)$$

We note that the $\hbar\omega_q$ is the energy of the phonon involved which is no greater than the ~ 0.1 meV. From the results above, we are able to extract the band gap from the x -axis intercept of the α^2 verses photon energy or $\alpha^{1/2}$ verses photon energy plot.

More information on the derivation and the optical properties associated to the free electrons can be found in chapter 2, 3 and 7 of reference 10.

2.4 Raman spectroscopy

2.4.1 General

Spectroscopy is a powerful tool to understand the physical properties of materials. Different spectral regions give different information of the material under characterization. A list of the physical origin and the corresponding spectroscopy for the study of it can be found in Table 2-1. Along with infrared (IR) spectroscopy, Raman spectroscopy is frequently used to understand the vibrational levels in the material. Raman spectroscopy and IR spectroscopy are complementary to each other in the sense that some vibrational modes are active to either one of them.

Even though IR spectroscopy and Raman spectroscopy measures the same physical origin, the experimental details are significantly different. Most of all, IR spectroscopy needs a source that generates an electromagnetic wave with an energy in the order of the vibrational modes, 10 meV to 1 eV. If there is an IR active vibrational mode, the vibrational mode will be excited by absorbing the electromagnetic wave with the same energy. However, in the case of Raman spectroscopy, a laser with a wavelength around the visible light region is used. The visible light excites Raman active phonons and loses the energy corresponding to it. As a result the wavelength of the reflected laser shifts by the amount of the lost energy. The wavelength of the reflected signal versus intensity data is retrieved and analyzed to study the vibrational modes.

The scattered light consists of two type of scattering. One is Rayleigh scattering which corresponds to the strong scattered light with exactly the same wavelength as the incident one. The other one is Raman scattering which is extremely weak compared to the Rayleigh scattering, approximately $\sim 10^{-5}$ times of it. Depending on whether the Raman scattering has lost or

| Spectroscopy | Range ($\tilde{\nu}$, cm^{-1}) | Energy (eV) | Origin |
|----------------------------------|---|-----------------------|---|
| γ -ray | 10^{10} - 10^8 | 10^6 - 10^4 | Rearrangement of elementary particles in the nucleus |
| X-ray (ESCA, PES) | 10^8 - 10^6 | 10^4 - 10^2 | Transitions between energy levels of inner electrons of atoms and molecules |
| UV-Visible | 10^6 - 10^4 | 10^2 -1 | Transitions between energy levels of valence electrons of atoms and molecules |
| Raman and infrared | 10^4 - 10^2 | 1- 10^{-2} | Transitions between vibrational levels (change of configuration) |
| Microwave | 10^2 - 10^1 | 10^{-2} - 10^{-3} | Transitions between rotational levels (change of orientation) |
| Electron spin resonance (ESR) | 1- 10^{-2} | 10^{-3} - 10^{-5} | Transitions between electron spin levels in magnetic field |
| Nuclear magnetic resonance (NMR) | 10^2 - 10^4 | 10^{-5} - 10^{-7} | Transitions between nuclear spin levels in magnetic fields |

Table 2-1 Spectral regions and their physical origin.

gained energy, it is either Stokes or anti-Stokes line. We define the frequency of the incident beam as ν_0 and the vibrational frequency of the excited phonon as ν_p . The Stokes line are red shift compared to the Rayleigh scattering, $\nu_0 - \nu_p$, while the anti-stokes are blue shift, $\nu_0 + \nu_p$.

The frequency shifts of Stokes and anti-Stokes line can be explained by understanding the physical origin of them. The derivation is done in a classical point of view. First, we consider the electric field (E) induced by the incident beam with a frequency ν_0 .

$$E = E_0 \cos 2\pi\nu_0 t \quad (2-18)$$

By the electric field, an electric dipole moment (p) will be induced which is related to the polarizability (α) of the material.

$$p = \alpha E = \alpha E_0 \cos 2\pi\nu_0 t \quad (2-19)$$

If the vibrational frequency of the phonons present in the crystal is ν_p , the related atoms will have a displacement (q) with an identical frequency

$$q = q_0 \cos 2\pi\nu_p t \quad (2-20)$$

Because of the vibration of the atoms, the polarizability of the material also changes slightly. Therefore, the Taylor expansion of the polarizability to the first order of the displacement gives the following.

$$\alpha(q) = \alpha_0 + \left(\frac{\partial \alpha}{\partial q} \right)_0 q + \dots \quad (2-21)$$

Substituting 2-20 and 2-21 in to 2-19 gives the following result.

$$\begin{aligned} p &= \alpha_0 E_0 \cos 2\pi\nu_0 t + \left(\frac{\partial \alpha}{\partial q} \right)_0 q_0 E_0 \cos 2\pi\nu_0 t \\ &= \alpha_0 E_0 \cos 2\pi\nu_0 t + \left(\frac{\partial \alpha}{\partial q} \right)_0 q_0 E_0 \cos 2\pi\nu_0 t \cos 2\pi\nu_p t \\ &= \alpha_0 E_0 \cos 2\pi\nu_0 t + \frac{1}{2} \left(\frac{\partial \alpha}{\partial q} \right)_0 q_0 E_0 \left[\cos 2\pi(\nu_0 + \nu_p)t + \cos 2\pi(\nu_0 - \nu_p)t \right] \end{aligned} \quad (2-22)$$

The final results show that the dipole moment oscillates in three different frequencies, ν_0 , $\nu_0 + \nu_p$ and $\nu_0 - \nu_p$, and thus, electric dipole radiation occurs in the same frequencies. Each corresponds to the Rayleigh scattering, anti-Stokes scattering and the Stokes scattering, respectively. It is also noticeable that the Raman scattering occurs only when $(\partial\alpha/\partial q)_0 \neq 0$.

For comparison, IR spectroscopy is discussed briefly. IR absorption is related to the dipole moment as well. However, while the origin of Raman intensity is due to the electric field induced dipole moment, IR absorption

occurs due to the dipole moment induced by normal coordinates. The dipole moment for this case is classically noted as μ . When the charge of each atom is e_i and the position of each atom as r_i , the dipole moment becomes as below.

$$\mu = \sum_i e_i r_i \quad (2-23)$$

When we consider the displacements of the atoms, the dipole moment can be also expanded.

$$\mu(q) = \mu_0 + \left(\frac{\partial \mu}{\partial q} \right)_0 q + \dots \quad (2-24)$$

As in the case of Raman spectroscopy, when $(\partial \mu / \partial q)_0 \neq 0$, the dipole moment oscillates in the frequency of the phonon and absorbs the IR electromagnetic wave with the same frequency.

In all, we find that IR and Raman spectroscopy is closely related to the electrical dipole moment. However, they have different rules to observe the phonon modes. Because of the different rules, IR spectroscopy and Raman spectroscopy are active to different types of vibration. For molecules that have a center of symmetry, normally the symmetrical vibrations are Raman active while it is IR inactive; meanwhile, the asymmetrical vibrations are Raman inactive while it is IR active. However, in a general situation, it is essential to check the conditions provided, for the case of Raman spectroscopy, $(\partial \alpha / \partial q)_0 \neq 0$. Here, we presented the polarizability to be isotropic, but in actual, this may not be the case. Thus, polarizability is represented as a tensor in general. Depending on the symmetry of the crystal, the components have a correlation to each other. Since, Raman scattering is related to the first derivative of the polarizability, our interest is the tensor $\alpha_{ij,k} \equiv (\partial \alpha_{ij} / \partial q_k)_0$ which is a rank three tensor. Here, i, j corresponds to the coordinates x, y, z and k

corresponds to the normal coordinates for the $3N-3$ vibration modes. This tensor is generally called as the Raman tensor and according to the space group of the crystal and the symmetry of the vibration, the form of the Raman tensor is restricted. Further discussions will be found in the next subchapter.

More informations and rigorous derivation can be found in reference 11, 12, 13.

2.4.2 Polarized Raman spectroscopy

Before proceeding to discussing polarized Raman spectroscopy, it is worthwhile to note vibrational modes in crystals. It is important to remember that a collection of atomic vibrations in a crystal can be viewed as a superposition of normal modes. Also, the lattice dynamics must obey the symmetry restrictions the space group has. Therefore, it is convenient to choose the normal modes as the ones that satisfy certain symmetry operations. The common notation for such normal modes is the Mulliken symbol. The definition of each symbol and an example are summarized in Table 2-2. First we must understand the principle rotation axis. For a symmetric point in a crystal, there are several symmetry operations and among them, the axis that contains the highest rotation symmetry is called the principle rotation axis.

Once we understand the irreducible representations of normal phonon modes in Table 2-2, the procedure of assigning normal modes to the Raman peaks by polarized Raman spectroscopy can be done. The remaining of this section will not focus so much on the mathematics and the detailed derivation, but more on the practical procedure of analyzing Raman spectroscopy results.

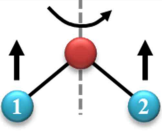
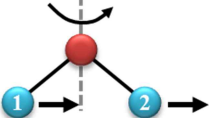
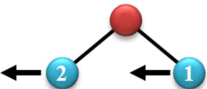
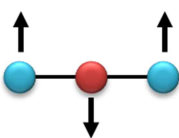
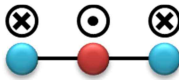
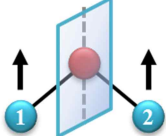
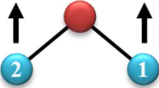
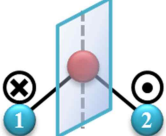
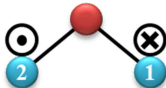
| | | |
|-------|--|--|
| A | Symmetric with respect to a $2\pi/n$ rotation around the n -fold principle rotation axis | |
| |  |  |
| B | Anti-symmetric with respect to a $2\pi/n$ rotation around the n -fold principle rotation axis | |
| |  |  |
| E | Doubly degenerate mode | |
| |  |  |
| T(F) | Triply degenerate mode | |
| X_g | <i>gerade</i> (German, even). Symmetric to inversion $\bar{1}$ | |
| X_u | <i>ungerade</i> (German, uneven). Anti-symmetric to inversion $\bar{1}$ | |
| X' | Symmetric to a mirror plane m which is perpendicular to the principle axis | |
| X'' | Anti-symmetric to a mirror plane m which is perpendicular to the principle axis | |
| X_1 | Symmetric to an additional 2-fold axis perpendicular to the principle axis, and if it is lacking, a mirror plane m parallel to the principle axis | |
| |  |  |
| X_2 | Anti-symmetric to an additional 2-fold axis perpendicular to the principle axis, and if it is lacking, a mirror plane m parallel to the principle axis | |
| |  |  |

Table 2-2 Mulliken Symbol notation and definition.

To execute polarized Raman spectroscopy, the experimental setup will be prepared as Figure 2-5. An easy way to represent the configuration of the polarized Raman experiment is the Porto notation. The incident beam direction, incident beam polarization direction, reflected beam direction, and the analyzed polarization direction is written in order. For example, in the case of the orientation in Figure 2-5, the incident beam is traveling in the direction of $-x$ and the polarization direction is y and the reflected beam is headed toward the $+y$ direction and the polarization is in the z direction. The Porto notation states this as $\bar{x}(yz)y$.

Under the assumption that the space group of the crystal is known, the procedure to perform polarization Raman spectroscopy and to assign the vibration modes is explained. Once the symmetry group is known, irreducible representation of all the possible vibration is determined. There are many references that list down the irreducible representation for all point groups and space groups. Here, all the relations and representations are found from the Bilbao Crystallographic Server (<http://www.cryst.ehu.es/>) [14].

As a specific example, we will consider the space group $Pm\bar{3}m$ (No. 221) and $Pnma$ (No. 62) in the case of a perovskite structure, ABO_3 . The

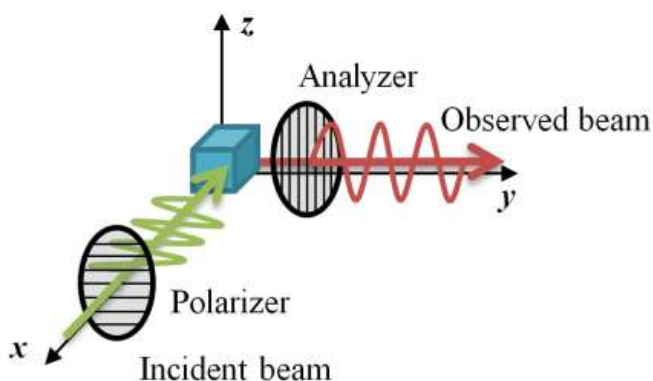


Figure 2-5 Schematic of polarized Raman spectroscopy

Wyckoff position and the atomic coordinates of each ions are as Table 2-3. From the information of the crystals, the irreducible representation of the vibration becomes known¹. Using the crystal information of a perovskite, the active modes and the number of each mode appears to be as Table 2-4. Considering the Wyckoff position of each atom and Table 2-4, the active vibration modes can be represented as below.

$$Pm\bar{3}m \text{ (No. 221)} : \Gamma_{vib} = 4T_{1u(IR)}$$

$$Pnma \text{ (No. 62)} :$$

$$\Gamma_{vib} = 10B_{1u(IR)} + 8B_{2u(IR)} + 10B_{3u(IR)} + 7A_g + 5B_{1g} + 7B_{2g} + 5B_{3g}$$

The results from above indicate that in the case of a perovskite with a $Pm\bar{3}m$ space group, there are no active Raman modes but only IR active modes (IR active modes are indicated with a parenthesis while all the others are Raman active modes for this case). On the other hand, in the case when the octahedral in the perovskite tilts, the space group lowers to $Pnma$ and a total of 24 Raman active modes appear. According to the symmetry relations, the Raman tensors are given as below for each vibration modes. It is important to note that the direction of x, y, z axis is in parallel to the primitive lattice vectors.

| A_g | B_{1g} | B_{2g} | B_{3g} |
|---|---|---|---|
| $\begin{pmatrix} a & 0 & 0 \\ 0 & b & 0 \\ 0 & 0 & c \end{pmatrix}$ | $\begin{pmatrix} 0 & d & 0 \\ d & 0 & 0 \\ 0 & 0 & 0 \end{pmatrix}$ | $\begin{pmatrix} 0 & 0 & e \\ 0 & 0 & 0 \\ e & 0 & 0 \end{pmatrix}$ | $\begin{pmatrix} 0 & 0 & 0 \\ 0 & 0 & f \\ 0 & f & 0 \end{pmatrix}$ |

¹ Bilbao Crystallographic Server (<http://www.cryst.ehu.es/>) → SAM (Spectral Active Modes) → Insert the crystal information (space group and Wyckoff positions).

| Ion | Wycoff position | Coordinates |
|--|-----------------|--|
| <i>Pm</i> $\bar{3}$ <i>m</i> (No. 221) | | |
| A | 1b | (1/2,1/2,1/2) |
| B | 1a | (0,0,0) |
| O | 3d | (1/2,0,0), (0,1/2,0), (0,0,1/2) |
| <i>Pnma</i> (No. 62) | | |
| A | 4c | (x,1/4,z), (-x+1/2,3/4,z+1/2), (-x,3/4,-z), (x+1/2,1/4,-z+1/2) |
| B | 4b | (0,0,1/2) (1/2,0,0) (0,1/2,1/2) (1/2,1/2,0) |
| O1 | 4c | (x,1/4,z), (-x+1/2,3/4,z+1/2), (-x,3/4,-z), (x+1/2,1/4,-z+1/2) |
| O2 | 8d | (x,y,z), (-x+1/2,-y,z+1/2), (-x,y+1/2,-z), (x+1/2,-y+1/2,-z+1/2), (-x,-y,-z), (x+1/2,y,-z+1/2), (x,-y+1/2,z), (-x+1/2,y+1/2,z+1/2) |

Table 2-3 Crystal information of perovskite with different space group.

| <i>Pm</i> $\bar{3}$ <i>m</i> (No. 221) | | | | | | | | | | | |
|--|----|-----------------|-----------------|-----------------|-----------------|----------------|----------------|-----------------|-----------------|-----------------|-----------------|
| | WP | A _{1g} | A _{1u} | A _{2g} | A _{2u} | E _u | E _g | T _{2u} | T _{2g} | T _{1u} | T _{1g} |
| IR | 1b | · | · | · | · | · | · | · | · | 1 | · |
| | 1a | · | · | · | · | · | · | · | · | 1 | · |
| | 3d | · | · | · | · | · | · | · | · | 2 | · |
| Raman | 1b | · | · | · | · | · | · | · | · | · | · |
| | 1a | · | · | · | · | · | · | · | · | · | · |
| | 3d | · | · | · | · | · | · | · | · | · | · |

| <i>Pnma</i> (No. 62) | | | | | | | | | | |
|----------------------|----|----------------|----------------|-----------------|-----------------|-----------------|-----------------|-----------------|-----------------|--|
| | WP | A _g | A _u | B _{1g} | B _{1u} | B _{2g} | B _{2u} | B _{3g} | B _{3u} | |
| IR | 4b | · | · | · | 3 | · | 3 | · | 3 | |
| | 4c | · | · | · | 2 | · | 1 | · | 2 | |
| | 8d | · | · | · | 3 | · | 3 | · | 3 | |
| Raman | 4b | · | · | · | · | · | · | · | · | |
| | 4c | 2 | · | 1 | · | 2 | · | 1 | · | |
| | 8d | 3 | · | 3 | · | 3 | · | 3 | · | |

Table 2-4 IR and Raman active modes in a perovskite

The intensity ($\Phi(k)$) of the Raman scattering is proportional to the square of the induced electric dipole moment. Therefore considering a scattered light which the polarization of the incident beam is given by e_{IB} , and the scattered beam as e_{SB} , the intensity of the Raman intensity can be expressed as

$$\Phi(k) = C \left| \sum_{i,j} e_{SB,j} \chi_{ij,k} e_{IB,i} \right|^2. \quad (2-25)$$

Following this relation, it is straight forward to find the polarization selection for Raman scattering. For example, in the case of a perovskite with a $Pnma$ space group, let's consider a situation where the incident beam is in the $-z$ direction with a x direction polarization and the scattered light that is being observed is projecting in the z direction with a y direction polarization. In Porto notation, it is $\bar{z}(x,y)z$. Considering equation 2-25 and the given Raman tensors, we find that only B_{1g} is observed with an intensity proportional to $|\chi_{xy}|^2 = d^2$. Also, we note that for the $\bar{z}(x,x)z$, only A_g mode is observable, and for $\bar{z}(x,y)z$, A_g is not observable but B_{1g} is observable.

2.4.3 Raman scattering intensity

Along with the Raman scattering intensity given above, we must consider the population of vibrational modes in the crystal. A quantum mechanical derivation is essential where the Boltzman distribution law is considered. According to it, the excited states are less populated than the ground states. This results in a stronger Stokes scattering than the anti-Stokes scattering. The resulting temperature dependent factor is called the Bose

factor and it is as below [15].

$$\Phi(k) = C \frac{1}{1 - \exp(-hc\tilde{\nu} / k_B T)} \left| \sum_{i,j} e_{SB,j} \chi_{ij,k} e_{IB,i} \right|^2 \quad (\text{Stokes})$$

$$\Phi(k) = C \frac{1}{\exp(hc\tilde{\nu} / k_B T) - 1} \left| \sum_{i,j} e_{SB,j} \chi_{ij,k} e_{IB,i} \right|^2 \quad (\text{Anti-Stokes})$$

This gives a ratio of Stokes to anti-Stokes scattering to be $\exp(hc\tilde{\nu}/k_B T)$. Since the temperature factor is not required in most analysis, in many cases the Bose factor is divided out from the acquired data.

Chapter 3

Experimental Details

3.1 Single crystal growth

Our research group reported that we have successfully grown BaSnO₃ single crystals by flux method [2]. The reported synthesis procedure was as the following. First, polycrystalline sample were synthesized by the solid state method. High purity BaCO₃, SnO₂, and La₂O₃ powders were weighed and mixed in a mortar. After pressing it in to a pellet, it was fired at 1250 °C for 9 hours. Another two rounds of grinding and firing at 1350 °C for 12 hours and 1450 °C for 24 hours followed. Polycrystalline BaSnO₃ was used as the seed material and it was mixed with Cu₂O flux with a molar ratio of 1:15. The mixed powder was placed in a Pt crucible and fired up to 1250 °C and then cooled down to 1210 °C in a rate of 0.1 °C/hr followed by a slow cooling to room temperature. However, undoped BaSnO₃ single crystals grown in such procedure resulted to have electron carriers up to $\sim 2\text{-}3 \times 10^{18} \text{ cm}^{-3}$ [3]. Our research group has continuously put effort to reduce the existing oxygen vacancy and eventually succeeded to supply oxygen during crystal growth by adding an oxidizer, KClO₄.

Adding an oxidizer during sample growth is an already known technique to supply oxygen to the material being synthesized. For an example, there were previous reports that superconducting materials such as Ca_{1-x}Sr_xCuO₂, YSr₂Cu₃O_y, and La_{1.7}Ca_{1.3}Cu₂O_y were successfully synthesized by using potassium chlorate, KClO₃, as an oxidizer during high pressure synthesis [16, 17, 18, 19]. We used a similar compound to KClO₃, potassium



Figure 3-1 BaSnO₃ single crystals grown with different molar ratio x of KClO₄ addition during flux growth

perchlorate (KClO₄) which is a well-known oxidizer in pyrotechnics [20]. However, there are hardly any reports that used an oxidizer to supply oxygen during flux growth. Probably, this is due to the fact that oxidizers may not just supply oxygen but leave impurities behind.

The single crystals studied in this study are all synthesized in the same condition that was developed in our research group. Only the amount of oxidizer was varied to control the amount of oxygen supplied. The seed polycrystalline BaSnO₃ was synthesized in the same procedure as before. In contrast to the previous recipe, a mixture of CuO and Cu₂O flux with the additional oxidizer, KClO₄, were altogether put into a Pt crucible by a molar ratio of 1: 50: x ($x=0-3$). The mixture of CuO and Cu₂O flux lowered the melting point so that the flux growth temperature range was as large as possible. The Pt crucible was fired in air up to 1230 °C and then slowly cooled down to 1060 °C followed by a normal cooling process to room temperature. Single crystals were successively grown and the color of the crystals made a clear group of two, a group of dark blue crystals ($x=0-1$) and the other group of bright yellow ($x=1.5-3$) as in Figure 3-1. Even though the as grown crystals are opaque to a certain degree, when the crystals are

polished to a plate shape, they become transparent as it appears in the bottom of Figure 3-1.

3.2 Structure analysis

The basic structure properties were studied by using a high power x-ray diffractometer which uses a single Cu $K_{\alpha 1}$ source (Empyrean™ PANalytical). The single crystals were carefully grinded and the XRD pattern was taken in both powder diffraction geometry and capillary geometry for comparison. For both cases, $1/8^\circ$ divergence slit, $1/4^\circ$ anti-scattering slit were used for best resolution. The powder x-ray diffraction took approximately 6 hours while in the capillary geometry, the whole measurement took 27 hours. To extract the lattice constants from the achieved data, Rietveld refinement was done by Fullprof.

At Pohang Accelerator Laboratory, X-ray Microdiffraction (XMD) facility at 4B beamline was used to do measurements on the single crystals. The energy of the white x-ray source ranged from 4-16 keV and the intensity was 10^{11} - 10^{12} photons/sec. A Bruker APEX II CCD detector (4096×4096 pixel) which has a size of 62 mm × 62 mm was placed 37 mm away from the sample. The orientation of the crystals was analyzed by XMAS (X-ray Microdiffraction Analysis Software), a freeware developed by the Advanced Light Source (ALS).

3.3 Electrical transport

Since the grown crystals vary in resistance largely, different measurement methods were applied. For the low resistance samples, the samples were measured in the four-probe scheme. Keithley 236 was used to supply current and probe the voltage. Meanwhile, the high resistance samples

were shaped into a thin plate and wires were contacted in the two-probe scheme. Keithley 617 was used to supply voltage and measure the current. The applied voltage was as high as 100 V. To measure the resistance in low temperature down to 10 K, the samples were loaded in a closed-cycle cryostat (Displex, Sumitomo Heavy Industries). Especially, when high resistance samples were loaded, the samples were cooled down until the measured current level reached the limit of Keithley 617 and then the cooling power was cut off so that the vibration of cryostat does not affect the measured low current. For the low resistance samples, the samples were shaped in to a thin bar and Hall measurement was taken in a physical property measurement system (PPMSTM Quantum Design) by applying a magnetic field up to 5 T. For the measurement, two lock-in amplifiers (Stanford Research Systems SR830) were used to measure the longitudinal and Hall voltage. The current was driven by a current calibrator (Valhalla 2500E).

3.4 Optical transmission

The optical transmission was measured with a Xenon lamp and a UV-visible-near-IR spectrometer (Stellonet EPP2000). There were no additional optical components to focus the source light. The samples were polished into a thin plate form by a successive use of sand papers and 50 nm colloidal silica suspension. Polishing and transmission measurement were repeated so that the absorption coefficient can be extracted. Also, the optical transmittance of BaSnO₃ single crystals were investigated in the range of Near-IR to UV with a Bomem DA8 Fourier transform spectrometer by the help of Dongmin Seo at University of Seoul.

3.5 Raman spectroscopy

A micro Raman system, XperRam200, from Nanobase was used for all Raman spectroscopy data. XperRam 200 uses a 16 mW 532 nm diode-pumped solid state laser which the power can be adjusted by a ND filter so that the power at the sample is approximately 2 mW. The microscope being used for XperRam 200 is an Olympus BX41 with a MPLFLN 40x objective lens. A scanner is present so that the sample under inspection can be scanned over a $200\ \mu\text{m} \times 200\ \mu\text{m}$ area. All the samples are measured in a back scattering geometry. There is a low frequency filter which cuts off the main Rayleigh scattering by approximately 99.9999 % which allows us to achieve the Raman scattering data down to $\sim 20\ \text{cm}^{-1}$. A XPE-200 VPHG (Volume Phase Holographic Grating) spectrometer with a 2300 lpmm (line per mm) grating is used along with an Andor iVac CCD which is cooled down to $-60\ ^\circ\text{C}$ thermoelectrically. Overall, the resolution is $1\ \text{cm}^{-1}$ per pixel. Additionally, a half-wave plate is placed on the laser side to control the incident beam polarization and an analyzer is placed on the spectrometer side to select a certain polarized direction.

For each sample, several spots were measured repeatedly and averaged. Sharp peaks due to cosmic ray and electrical noise were manually taken out. Afterwards, the scattering intensity was calculated accordingly to that explained in chapter 2.4.3. Additionally, for polarized Raman spectroscopy, it must be known that there is a polarized direction dependency in the response of the spectrometer and CCD unit. The parallel polarized signal shows a higher response compared to the 90° polarized signal by 1 to 0.6. Thus, the achieved data must be normalized for comparison.

Chapter 4

Results and Discussions

4.1 Structure analysis

4.1.1 X-ray diffraction

The x-ray diffraction for carefully grinded BaSnO_{3-x} single crystals was taken both in powder diffraction geometry and capillary geometry. The results are shown in Figure 4-1. There are no apparent difference between the $x=0$ and $x=2$ BaSnO_3 single crystals. However, there is a minor difference in the peak amplitude. The powder diffraction geometry clearly sense weak peaks such as (100) and (111) while in the case of capillary geometry, those peaks are not distinguishable from the background signal. This is due to the fact that only a small amount of single crystal powder is used for the capillary geometry measurement. However, capillary geometry measurement reduces any preferable orientation the powder has and results in a better agreement with the simulated intensities. Rietveld refinement was performed by Fullprof with the space group fixed as $Pm\bar{3}m$. The extracted lattice parameters appear to be identical for all cases, $a=b=c=4.117 \text{ \AA}$. Therefore, from the perspective of a laboratory x-ray diffractometer, the BaSnO_3 single crystal has an identical structure, cubic perovskite structure, regardless of the addition of KClO_4 . However, laboratory x-ray sources have limited intensity that can be radiated upon the crystal. Thus, any small peaks due to a small change in symmetry or by distortion may not be observable in x-ray diffraction experiments simply because of intensity problems.

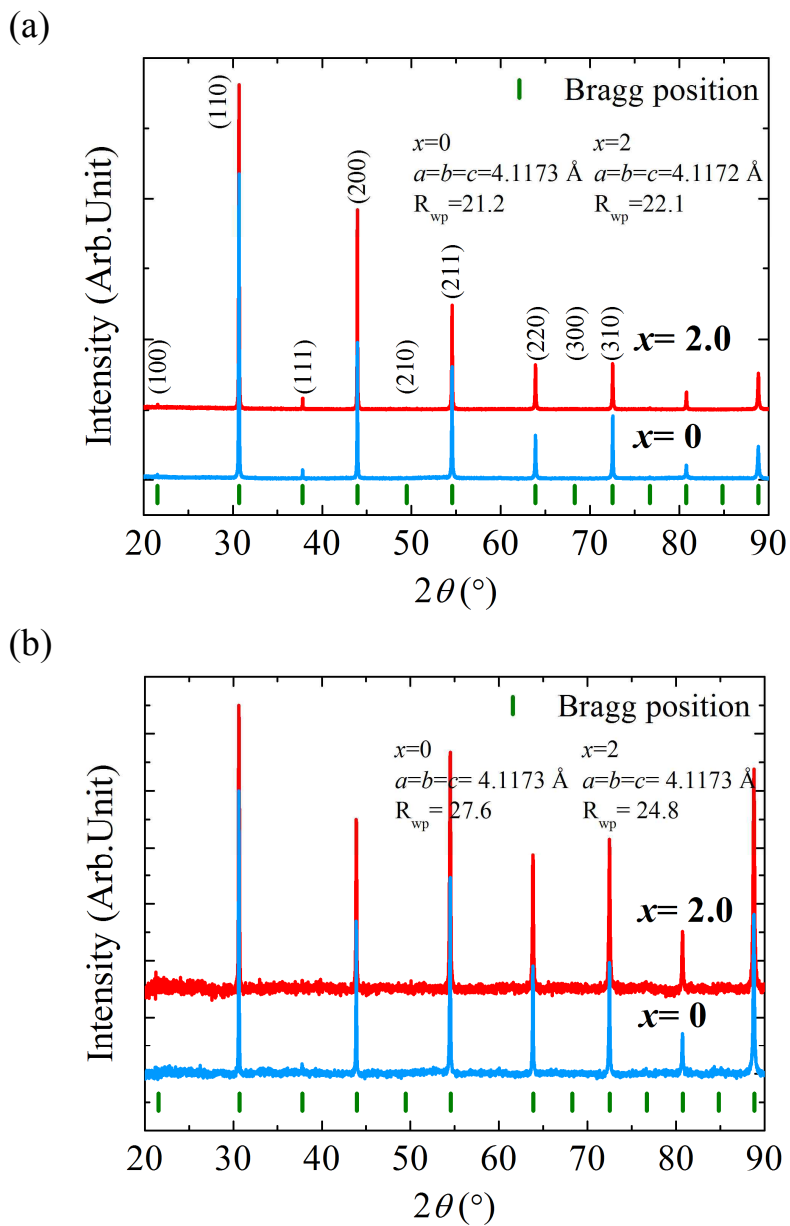


Figure 4-1 X-ray diffraction results in (a) powder diffraction geometry and in (b) capillary diffraction geometry

4.1.2 X-ray microdiffraction

Even though the previous result shows that there is no structural differences between the $x=0-1$ $\text{BaSnO}_{3-\delta}$ crystals and the $x=1.5-3$ crystals, it is worthy to try a structural study in a high intensity and high resolution equipment. There are many options, but we neglect powder measurement because grinding the single crystals may cause unwanted structural distortion. Therefore, some of the choice left is x-ray four circle diffractometer, x-ray Laue diffractometer, neutron four circle diffractometer, and so on. Here, we measured x-ray microdiffraction which the principle is equal to x-ray Laue diffraction except the fact that the x-ray is focused into a micrometer size spot.

The x-ray microdiffraction 4B beamline at Pohang Accelerator Laboratory provides a photon intensity of $10^{11}\sim 10^{12}$ photons/sec. Therefore, the measurements take less than a couple seconds. The strong x-ray intensity and the large two-dimensional CCD allow many peaks to be observed at a single shot. The results are as shown in Figure 4-2.

The x-ray microdiffraction results do not show a noticeable difference. As seen in Figure 4-2, the main Laue spots are identical in position. The written indices below the peaks are the indices corresponding to the cubic perovskite structure. There are small Laue spots that are different between the $x=0$ and $x=2$ BaSnO_3 single crystal; however, they do not appear consistently over several Laue patterns taken in different spatial positions. Overall, as the previous x-ray diffraction results, x-ray microdiffraction at a light source indicates that there is no structural difference between $x=0$ and $x=2$ BaSnO_3 single crystals.

4.2 Electrical transport

4.2.1 Temperature dependent resistivity

The temperature versus resistivity measurement was done in low temperature region. At room temperature, BaSnO₃ single crystals had distinctive resistance values. Interestingly, the crystals with blue color ($x=0-1$) had low resistance while the crystals which are yellow ($x=1.5-3$) had high resistance that could not be measured by a conventional multimeter. The crystals that have low resistance in room temperature were measured in four-probe method. The crystals with high resistance which could not be measured by a multimeter were measured in two-probe method. The low resistance crystals were measured from the base temperature of the cryostat while the high resistance crystals were measured from 150 K because the resistance of the sample surpassed the maximum limit of the electrometer (KE617). The results are shown in Figure 4-3.

It is clear that the single crystals can be divided in to two groups which are identical to the two groups observed in the color of the crystals. For the low resistance group, the resistivity is as low as ~ 1 m Ω cm. The resistivity systematically increases as the ratio of KClO₄ increases. When the resistivity reaches ~ 1 Ω cm, a slight increase of KClO₄ dramatically changes the resistivity to $>10^{10}$ Ω cm. The absolute value of the resistivity among the high resistance group does not change systematically as the ratio of KClO₄ increases.

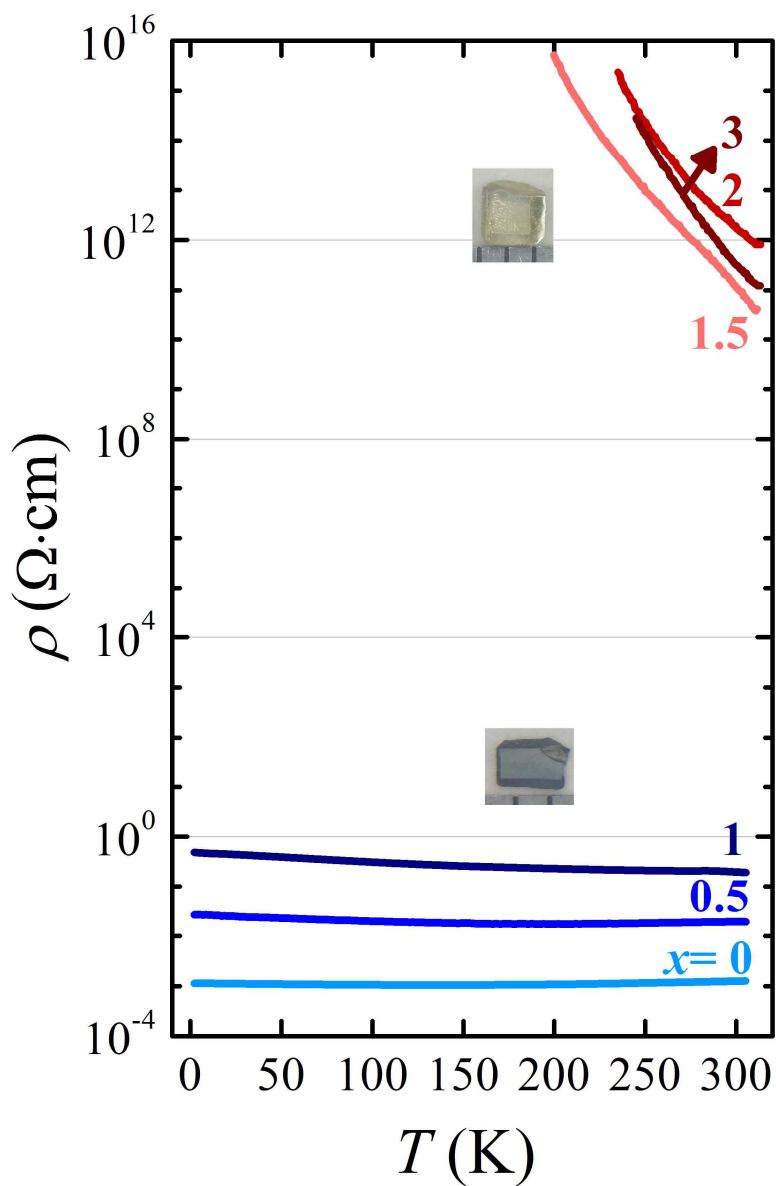


Figure 4-3 Temperature dependent resistivity measurement on BaSnO_3 single crystals with different molar ratio ($x=0-3$) of KClO_4 during single crystal growth.

From the temperature dependent resistivity measurement, it is clear that the supply of oxygen during crystal growth increases the resistivity of the BaSnO₃ single crystals. Therefore, it implies that the oxygen vacancy is reduced by the addition of KClO₄ during flux growth. To ensure that electrons carriers truly reduced, several inspections are repeated.

Before we continue, the Arrhenius plot is taken for the high resistivity samples. The Arrhenius plot is useful to extract the thermal activation energy. The relation between the carrier concentration (n) and the thermal activation energy (E_a) is related as the following.

$$n(T) = n_0 e^{-\frac{E_a}{k_B T}} \quad (4-1)$$

From Equation 2-6, we know that $\sigma = ne\mu$. Therefore, by substituting the equation above, the relation becomes

$$\sigma(T) = n_0 e^{-\frac{E_a}{k_B T}} e\mu(T) . \quad (4-2)$$

We take the logarithm and express the equation by resistivity. Also, we assume that the mobility is temperature independent.

$$\ln(\rho) = \frac{E_a}{k_B T} - \ln(n_0 e\mu) \quad (4-3)$$

The Arrhenius plot is to plot $\ln(\rho)$ versus $1/k_B T$. Thus, the slope will indicate the activation energy of the carriers.

Figure 4-4 shows the Arrhenius plot for the high resistivity samples. Even though the room temperature resistivity appears to not have systematic behavior in respect to the increase of KClO₄, the activation energy clearly shows an increasing behavior. Since the band gap of BaSnO₃ is known to be ~3 eV, the origin of the measured excited carriers seems not to be the intrinsic

carriers. However, the exact source of carriers that becomes activated at high temperature remains unclear.

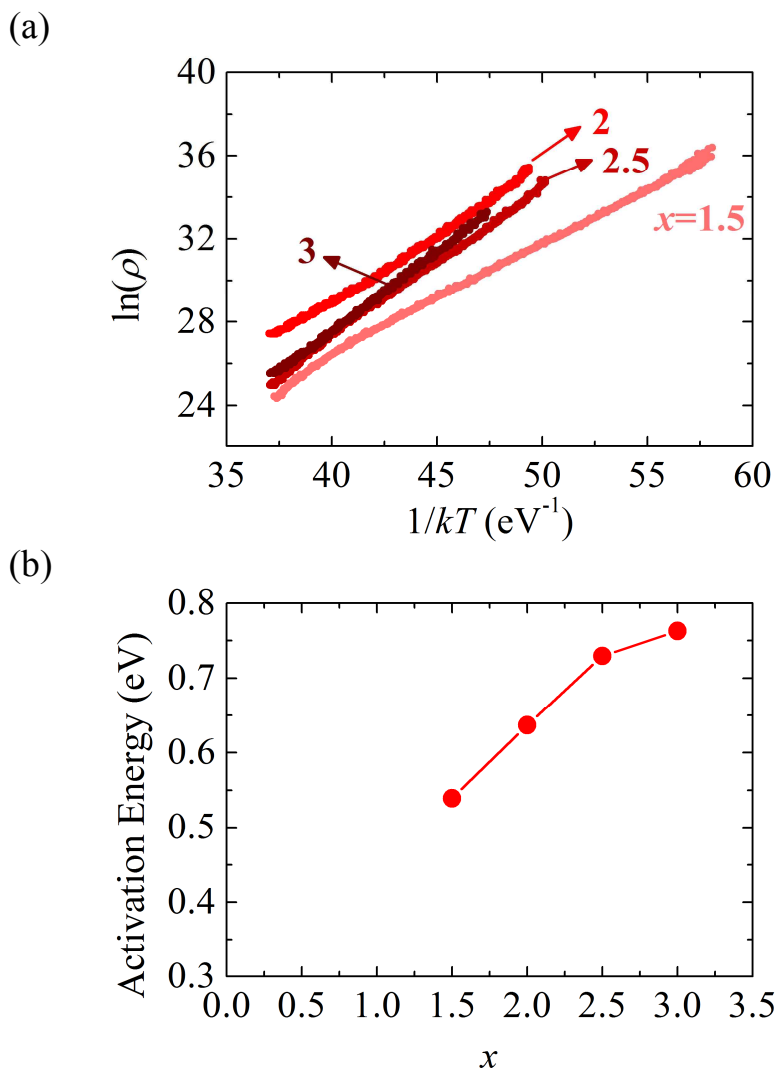


Figure 4-4 (a) Arrhenius plot for the BaSnO₃ single crystals with high resistivity ($x=1.5-3$) (b) Activation energy versus molar ratio of KClO₄ to BaSnO₃ during flux growth.

For the crystals with low resistivity, the Hall measurement was taken under a magnetic field sweep from -5 T to 5 T. A clear linear relationship between the Hall voltage and the applied magnetic field were observed. Therefore from the slope, we are able to extract the carrier concentration and the carrier type by equation 2-8. Once the carrier concentration is known, the mobility is calculated from equation 2-6. The carrier type has been confirmed to be an electron carrier which is consistent to the previous report [3]. The carrier concentration and mobility verses KClO_4 molar ratio data is given in Figure 4-5. The carrier concentration shows a slowly decreasing behavior as the ratio of KClO_4 increases. When the molar ratio is above $x=1$, a sudden metal-insulator transition occurs. N. F. Mott has explained the transition from a metal to insulator and he suggested a criterion to explain the condition of the transition [21]. For the case where the effective Bohr radius is a_H^* , the critical carrier concentration (n_c) that the metal-insulator transition occurs has a following relation.

$$n_c^{1/3} a_H^* = 0.26 \pm 0.05 \quad (4-4)$$

The relation between the effective Bohr radius and the Bohr radius of a hydrogen atom (a_0) is mediated by the relative permittivity (ϵ_r) and the effective mass (m^*) of the electron in the material being under consideration. The effective Bohr radius is calculated to be as below where m_0 is the electron rest mass.

$$a_H^* = \frac{a_0 \epsilon_r}{m^*/m_0} \quad (4-5)$$

For the case of BaSnO_3 , the reported effective mass of the electron carrier varies widely. The calculated theoretical effective mass ranges from 0.06 to $0.96 m_0$ [2, 22, 23, 24, 25, 26]. The electron effective mass extracted from

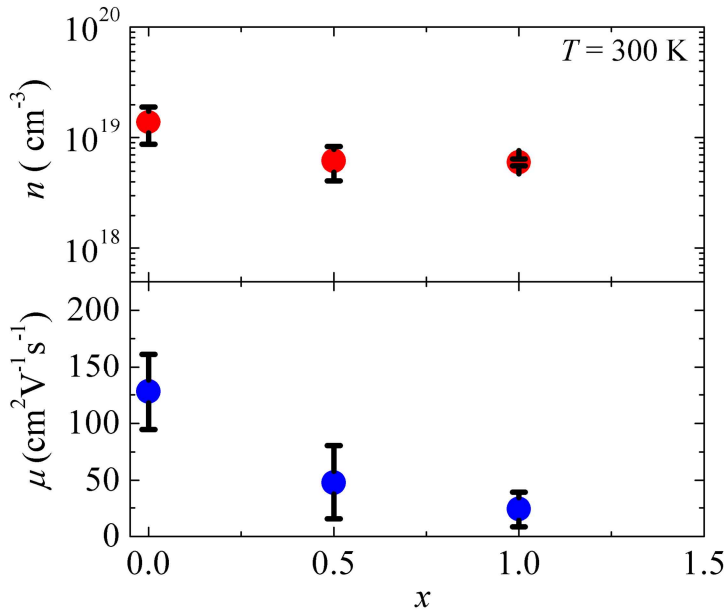


Figure 4-5 Hall measurement results of low resistivity BaSnO₃ single crystals ($x=0-1$)

IR spectroscopy is $0.35 m_0$ [27]. The relative permittivity was measured to have an average of 16.1 in the high resistivity samples ($x=1.5-3$). Calculating the effective Bohr radius with the given values is 23 \AA . Therefore, by Mott criterion, the critical carrier concentration is $1.2 \times 10^{18} \text{ cm}^{-3}$. The carrier concentration in the low resistivity BaSnO₃ crystals ($x=0-1$) are greater than the calculated critical carrier concentration satisfying the Mott criterion. However, we were not able to observe a gradual crossover in the critical limit but rather an abrupt jump to the insulating single crystal phase. This maybe indicating that a certain atmospheric pressure or other environmental condition is required to have the oxygen vacancies filled up and when KClO₄ molar ratio is above the limit, the condition is satisfied.

Meanwhile, when we take a look on the electron carrier mobility, a more significant drop is observed. This indicates that the scattering source

within the crystal is increasing and it may also imply that K or Cl impurities are playing the role of it. The systematic increase of resistance among $x=0-1$ in Figure 4-3 is mostly due to the decrease of the carrier mobility instead of the reduction of carriers. In other words, until a certain critical molar ratio of KClO_4 is reached, the oxygen vacancy does not seem to decrease but the carrier mobility decreases due to the increase of scattering sources. Once, the critical molar ratio of KClO_4 is supplied, the supplied oxygen is effectively introduced in to the crystal giving a highly insulating BaSnO_3 single crystal

4.3 Optical transmission

The optical transmission measurement was taken to observe whether the free carriers are reduced by the addition KClO_4 . Here, we measured the transmittance from near-IR to UV, but if we extend the region to far-IR, it would be possible to extract the carrier concentration from the results. Also, optical transmission data allows us to know the optical band gap from it. Therefore, whether the addition of oxidizer affects the optical band gap can be studied. Additionally, the existence of impurity can be noticed if a mid-gap state appears in the transmission data. However, the absence of mid-gap state does not solely mean that the sample is free from impurity.

The optical transmittance measurement results in the near-IR to UV region are shown in Figure 4-6 (a). At once, the distinct behavior among the BaSnO_3 single crystals is observable. The transmittance of the high resistivity single crystals extends down to less than 2000 cm^{-1} . On the other hand, the low resistivity single crystals show a drastic drop starting from 10000 cm^{-1} . This is due to the free carrier absorption mentioned in equation 2-16. To see whether the absorption coefficient follows the predicted $\alpha \propto \omega^{-\beta}$ behavior where $\beta=2$ in the ideal case, the absorption coefficient was extracted and plotted in a log-log plot (Figure 4-6 (b)). We note that because the absorption coefficient needs the transmittance data and the reflectance data all together to be calculated, we used an optical spectra software RefFIT to acquire the absorption coefficient through fitting. The parameter for ϵ_{opt} in equation 2-14 was fixed to the value of the high resistivity crystals for all fitting. When we see the results in Figure 4-6 (b), the absorption coefficient of low resistivity crystals follow the $\alpha \propto \omega^{-2}$ tendency fairly well. The transmittance and absorption coefficient values appear not to be systematically changing in the case of $x=0-1$ crystals. However, we believe this is due to the limited number

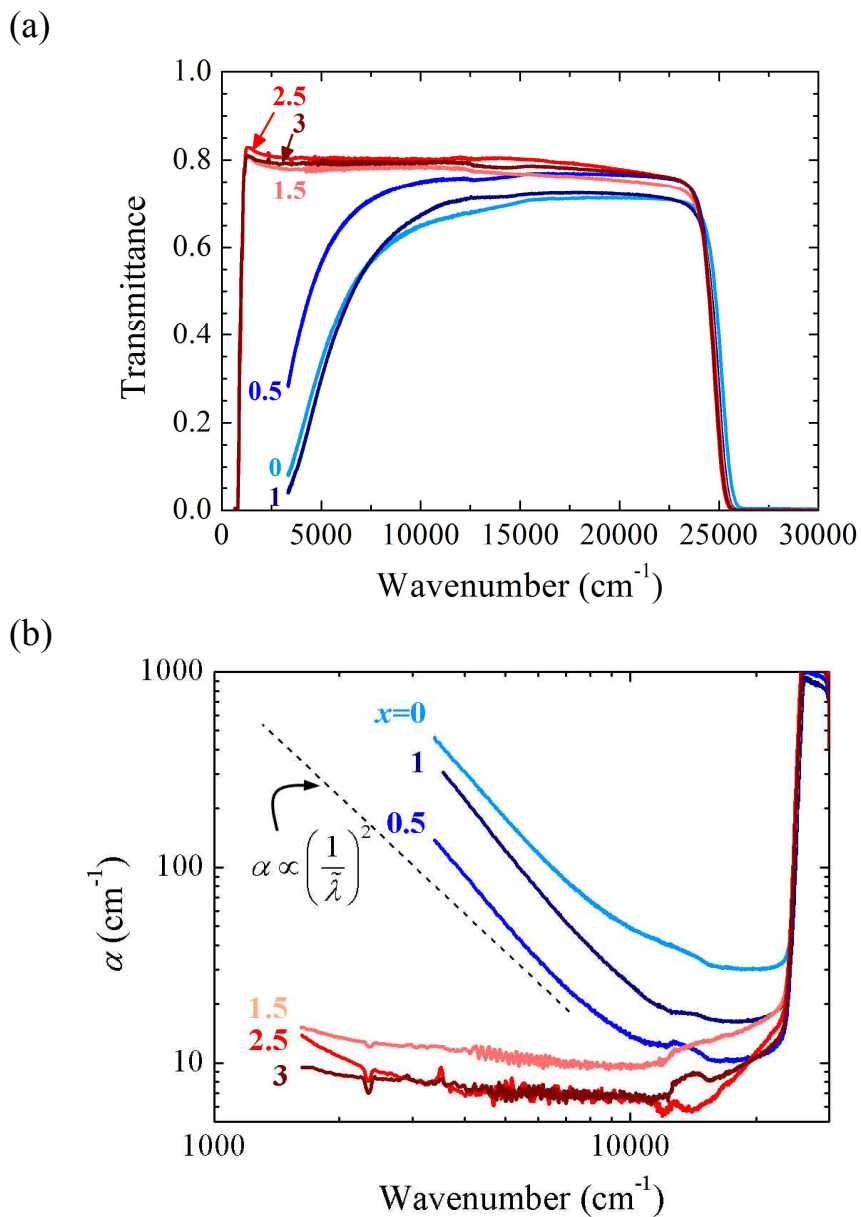


Figure 4-6 (a) Optical transmittance results in the region of near-IR to UV. (b) Absorption coefficient versus wavenumber extracted by RefFIT. The dashed line indicates the predicted slope by free carrier absorption.

of samples and measurement errors. At the moment, repeated measurement on several crystals is required to achieve a reliable data set.

The optical transmittance measurement was also taken in the visible region by using a xenon lamp and a near-IR-UV spectrometer. The crystals were grinded in different thickness so that the absorption coefficient can be calculated even without measuring the reflectance. The method is as the following. We consider the case where the source being used is an incoherent light. Also, when we assume that the reflectivities of the front and back surfaces are equal to R , the transmission T follows the following equation where α is the absorption coefficient and l is the thickness of the plate.

$$T = \frac{(1-R)^2 e^{-\alpha l}}{1-R^2 e^{-2\alpha l}} \quad (4-6)$$

In a strongly absorbing material $\alpha l \gg 1$, and the equation above reduces to:

$$T = (1-R)^2 e^{-\alpha l} \quad (4-7)$$

By dividing two successive transmittance measurements with different sample thickness l_1 and l_2 , the absorption coefficient can be known as below.

$$\frac{T_1}{T_2} = e^{-\alpha(l_1-l_2)} \quad (4-8)$$

Thus,

$$\alpha = -\frac{\ln(T_1/T_2)}{l_1-l_2}. \quad (4-9)$$

With equation 4-9, the absorption coefficient is calculated. Figure 4-7 shows the result by plotting the same data in α^2 verses photon energy and $\alpha^{1/2}$ verses photon energy. From equation 2-17, we know that by applying linear extrapolation to the linear region, the x -axis intercept will indicate the optical

band gap for each case. For both α^2 versus photon energy and $\alpha^{1/2}$ versus photon energy cases, a well-defined linear region is present. Therefore, by this result we are not able to determine exactly which transition is dominant. Previously, Kim *et al.* has reported a similar result in (Ba,Lu)SnO₃ and in undoped BaSnO₃ single crystals. There they mentioned that the calculated band structure indicate an indirect band gap in BaSnO₃. However, because the optical selection rule is satisfied at the Γ point (transition from O 2p to Sn 5s), a direct optical transition appears strongly [2]. The extrapolated optical band gap values are given as a table in Figure 4-7. Even though whether the transition is direct or indirect is not clear from this data set, there is a

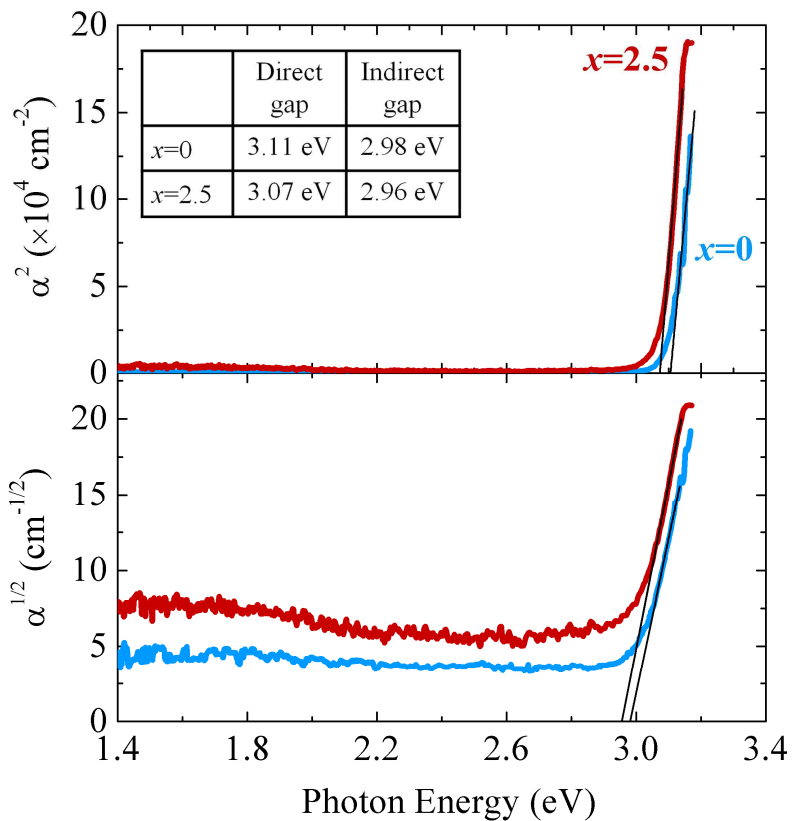


Figure 4-7 Optical transmittance measurement results in visible-UV region.

consistent result among the achieved optical band gap. The high resistivity single crystal has a smaller optical gap compared to the low resistivity single crystal by ~ 0.04 eV. A similar phenomenon was observed by Kim *et al.* In their case, the optical band gap of (Ba,La)SnO₃ was greater than the undoped BaSnO₃ optical band gap by ~ 0.23 eV. This difference was attributed to Burstein-Moss shift.

Burstein-Moss shift occurs in a degenerate semiconductor with a narrow conduction band. Qualitatively, even an electron doping level not so great will easily occupy the lower part of the narrow conduction band because it has small density of states. Therefore, the electrons from the valence band cannot make a transition to the conduction band minimum. Instead, additional photon energy is required to make a transition from the valence band maximum to the minimum unoccupied state in the conduction band. When we define ΔE as the energy difference of the conduction band minimum and the minimum unoccupied state, the relation with the carrier concentration n and the effective electron mass m^* is as below.

$$\Delta E = \frac{\hbar^2}{8m^*} \left(\frac{3n}{\pi} \right)^{2/3} \quad (4-10)$$

In the case of the measured $x=0$ BaSnO₃ single crystals, the carrier concentration is $n \sim 10^{19}$ cm⁻³ from Hall measurement results and the effective mass is $m^* \sim 0.4 m_0$ from previous report [7]. When these values are substituted, the optical band gap shift is calculated to be $\Delta E \approx 42.3$ meV. This is in good agreement with the measured results, $\Delta E \approx 0.04$ eV. Therefore, the decrease of optical band gap in insulating BaSnO₃ can be explained by the fact that the carrier concentration in the conduction band has been reduced.

4.4 Raman spectroscopy

4.4.1 BaSnO_{3-δ} Single crystals

Raman spectroscopy is a sensitive tool to observe the vibration modes a material has. Therefore, it is also sensitive to the structure. Although the x-ray diffraction results didn't show any difference among the crystals, there may be local distortion that cannot be detected by x-ray diffraction. This is because x-ray observes the global symmetry the crystal has while Raman spectroscopy is sensitive to local symmetry. For example, Raman spectroscopy can observe the vibration modes of even gas and liquid while x-ray diffraction cannot. Through Raman spectroscopy, we inspected if there are any vibration mode differences among the crystals grown with and without the addition of an oxidizer.

The single crystals that are extracted after flux growth may have flux remaining on the surface even after melting the flux in nitric acid. Therefore, the single crystals were cleaved so that a clean surface could be examined. The incident beam and reflected beam were in the [001] direction. The depolarized reflected beam was measured. For each measurement, the CCD was exposed for 15 minutes and repeated measurement results were averaged out. Figure 4-8 show the results.

Clearly there is a big difference between the crystals that has electron carriers ($x=0-1$) and that does not have carriers ($x=1.5-3$). The single crystals with electron carriers have strong Raman peaks at 138, 248, 615, and 650 cm^{-1} while the single crystals without electron carriers do not have it. It is interesting that a distinct difference in Raman spectra is observed while the x-ray diffraction pattern does not show any difference.

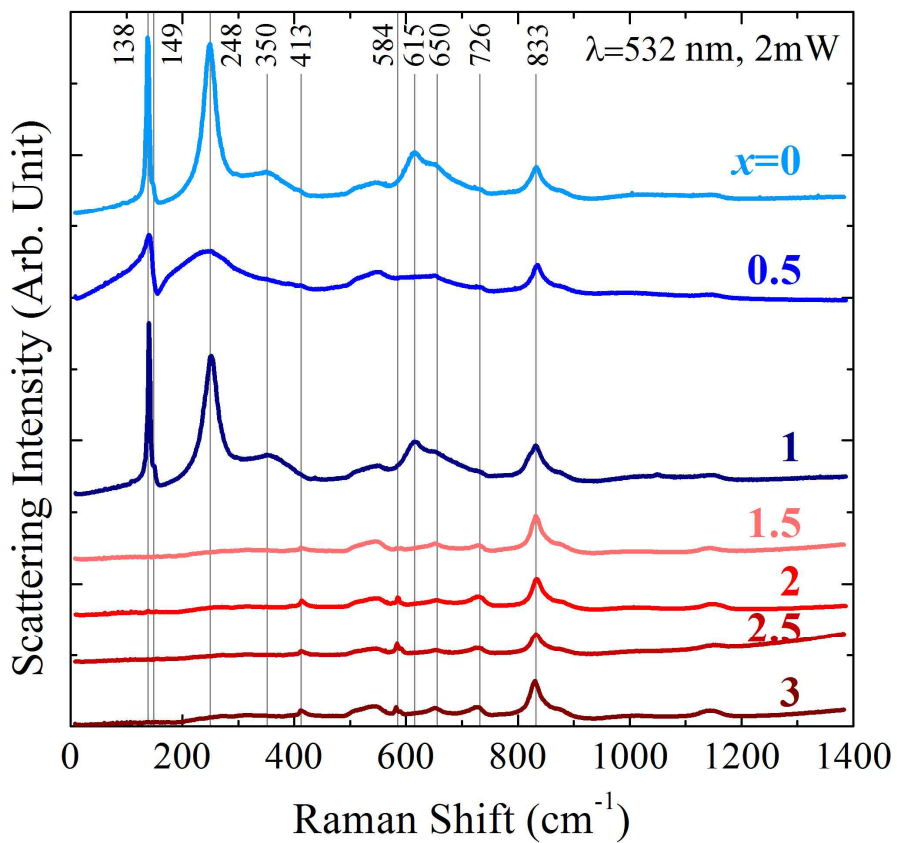


Figure 4-8 Depolarized Raman spectroscopy on BaSnO_{3-x} single crystals.

In the case of BaSnO_3 , the space group is known to be $Pm\bar{3}m$ (No. 221) which does not have any Raman active modes as it was discussed in chapter 2.4.2. Therefore, the strong Raman peaks observed in the $x=0-1$ crystals cannot be assigned to the vibration modes in $Pm\bar{3}m$ space group. This indicates that the single crystals with electron carriers may be distorted from the cubic structure. For example, by the octahedral tilting the structure symmetry can be lowered to either a tetragonal, rhombohedral or orthogonal structure.

To assign the unknown Raman peaks, polarized Raman spectroscopy was taken. First, several space group candidates were selected according to the possible symmetry lowering a perovskite have. In many other oxide perovskites, it has been observed that the space groups changes from a low symmetry one to a higher symmetry space group as the temperature is increased. From the previous results, the symmetry change has been observed to follow one of the case appeared in Figure 4-9 [28, 29]. When we take $R\bar{3}c$ and $Pnma$ as our candidate, we can expect the Raman active modes as in

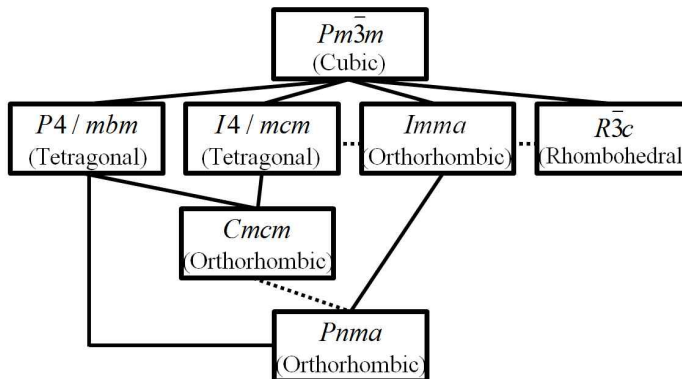


Figure 4-9 Space group relations in perovskites that goes through phase transitions. Continuous phase transitions are in solid lines and first order transitions in dotted lines.

| $R\bar{3}c$ | | | | | $Pmna$ | | | | |
|-----------------------|-------------|-------|--------------|-------|-----------------------|-------------|----------|--------------|----------|
| Orientation | 0° rotation | | 45° rotation | | Orientation | 0° rotation | | 45° rotation | |
| Modes Polarization | A_{1g} | E_g | A_{1g} | E_g | Modes Polarization | A_g | B_{1g} | A_g | B_{1g} |
| $\bar{z}(x,x)z$ | O | O | O | O | $\bar{z}(x,x)z$ | O | O | O | · |
| $\bar{z}(x,y)z$ | · | O | · | O | $\bar{z}(x,y)z$ | O | · | · | O |
| $\bar{z}(y,y)z$ | O | O | O | O | $\bar{z}(y,y)z$ | O | O | O | · |

Table 4-1 Raman active modes for the case of $R\bar{3}c$ and $Pmna$ perovskites. The 0° rotation is the case where $\vec{x} \parallel [100]_{pc}$ and the 45° rotation is the case where $\vec{x} \parallel [110]_{pc}$. Here, the subscripts indicate that the directions are in pseudocubic notation.

Table 4-1. Therefore, by changing the direction of the incident beam and the polarization direction, it is possible to narrow down the space group of the single crystal.

Figure 4-10 shows the orientation of the crystal and the polarized Raman results. All results show a similar behavior. In the case of $\bar{z}(x,x)z$, strong Raman peaks are apparent for both cases, when the incident beam enters in an angle of 0° and in 45°. However, when the cross polarized signal is obtained, $\bar{z}(x,y)z$, almost no signal is detected. From Table 4-1, E_g or B_g modes should show a Raman peak when the cross polarization signal is taken. Meanwhile, A_g modes will show polarization dependent Raman signal as it appear in Figure 4-10. The results leads to a conclusion that all observed Raman peaks are A_g modes; however, this raises several questions. The possible Raman active modes in the two structures are as below.

$$R\bar{3}c \text{ (No. 167): } \Gamma_{Raman} = A_{1g} + 4E_g$$

$$Pmna \text{ (No. 62): } \Gamma_{Raman} = 7A_g + 5B_{1g} + 7B_{2g} + 5B_{3g}$$

The angle dependent polarized Raman scattering results indicate that there is a

high possibility that $x=0$ BaSnO₃ single crystal has a $R\bar{3}c$ symmetry. But, $R\bar{3}c$ allows only one A_{1g} mode. Therefore, either the space group is not $R\bar{3}c$ or some of the peaks should be E_g modes. When we assume that the space group is *Pnma*, the A_g modes can be explained but the absence of B_{1g}, B_{2g}, and B_{3g} is not clear. At the moment, the symmetry of the crystal cannot be pinned down to a certain space group

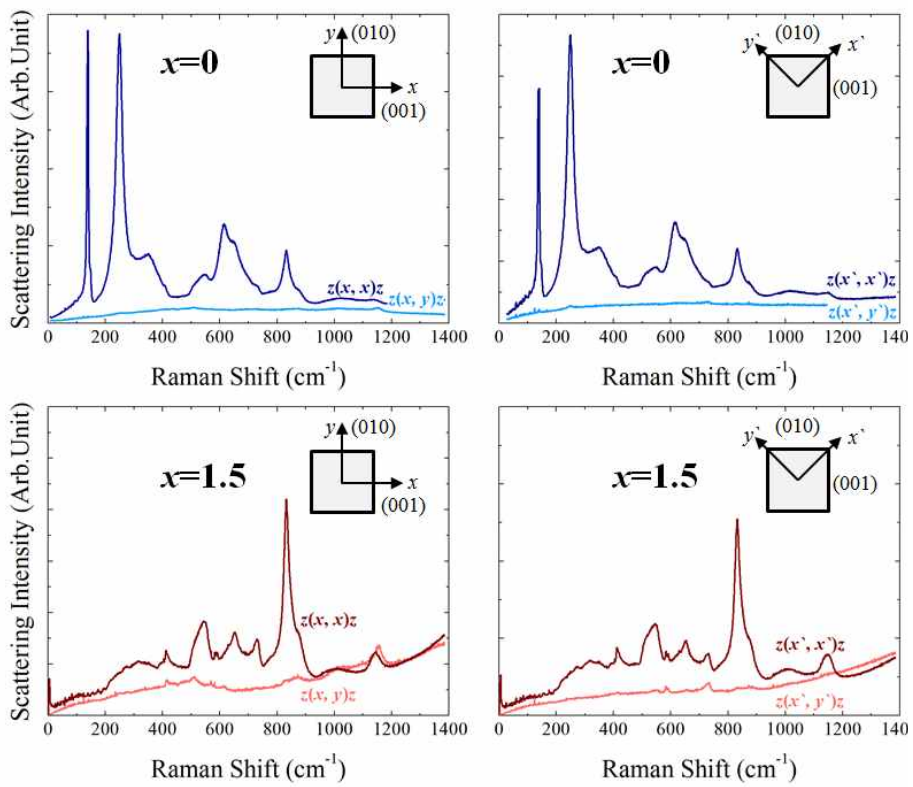


Figure 4-10 Polarized Raman spectroscopy on $\text{BaSnO}_{3-\delta}$ single crystals.

The measured $\text{BaSnO}_{3-\delta}$ Raman peaks are not clearly assigned to specific vibration modes. For the case of $x=0$ $\text{BaSnO}_{3-\delta}$ single crystals, the strong Raman peaks are thought to be first order Raman peaks. Meanwhile, the oxygen supplied $x=2$ BaSnO_3 single crystals are thought to be ideally cubic and the measured Raman peaks are thought to be second order Raman peaks. However, the 833 cm^{-1} peak seems to be intense and the 413 and 584 cm^{-1} are sharp. To assure that these peaks are not originated from any impurities due to the flux or other second phase, Raman spectrum of polycrystalline BaSnO_3 pellet was taken. As in Figure 4-11, most of the Raman peaks, except the peak at 584 cm^{-1} , identically appear in the BaSnO_3 polycrystalline pellet. This indicates that the peaks observed in the single crystal are intrinsic Raman peaks. Also, this shows that the single crystals grown with KClO_4 has an identical crystal structure with the undoped BaSnO_3 polycrystalline sample while the single crystals grown without KClO_4 during flux growth is somewhat different in terms of structural property.

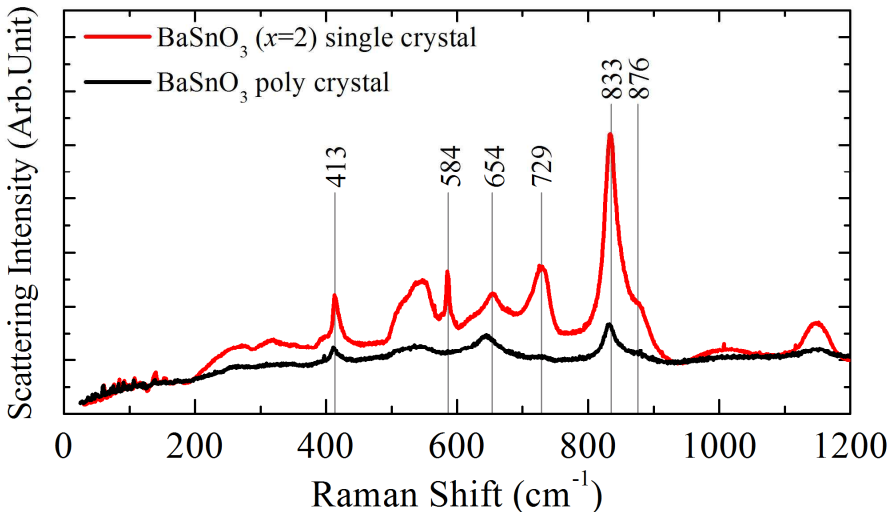


Figure 4-11 Depolarized Raman spectroscopy on BaSnO_3 single crystal ($x=2$) and poly-crystal.

4.4.2 External effect on crystal structure

In many cases, samples that are under investigation go through a polishing procedure so that a specific size or a certain surface roughness is achieved. Especially, for optical measurements the samples are often polished finely to a point where the surface roughness is within a nanometer scale. In this procedure, there is high possibility that the surface structure becomes distorted. Raman spectroscopy is much more sensitive to the surface status than IR spectroscopy since it uses a shorter visible light source. We executed Raman spectroscopy on BaSnO₃ single crystal as it is grown first. Afterwards, the surface was finely polished with a sand paper and then we measured Raman spectroscopy. Lastly, the polished crystal was annealed at 1000 °C for 12 hours under oxygen gas flow. Once the crystal was cooled back to room temperature Raman spectroscopy was taken. The results are shown in Figure 4-12.

After polishing, more Raman peaks emerges at several different regions. It is not clear to which space group the structure has been changed to. However, we conjecture that the polishing caused the octahedra to tilt more and result in a lower symmetry space group. The overall Raman spectrum looks similar to SrSnO₃ which is an orthorhombic perovskite with a space group *Pnma* [30]. If we assume that the Raman peaks do not differ much from SrSnO₃, we are able to make a naïve guess on what modes the Raman peaks are. The peaks at 87 and 109 cm⁻¹ are thought to be due to O-Sn-O bending modes within the *ab* plane while the movements of Ba atoms are in the *b* direction. Also, the peaks at 628, 678, and 726 cm⁻¹ is thought to be related to Sn-O stretching modes. It is interesting that in reference 30, the theoretical calculation predicts a set of bands near 380 cm⁻¹ and a band between 640 and 710 cm⁻¹ in SrSnO₃ which also explains the distorted Raman spectrum.

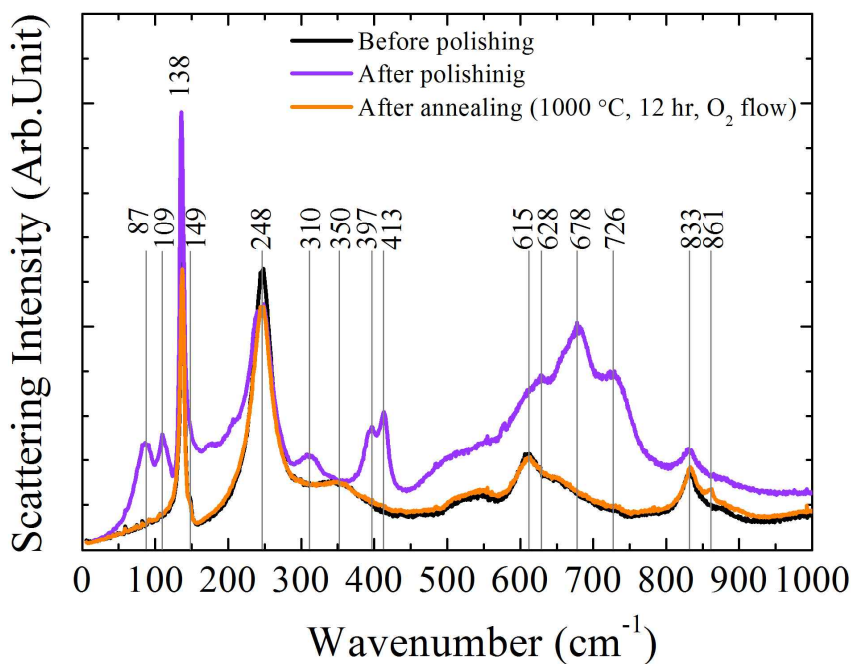


Figure 4-12 Polishing and subsequent O₂ annealing effect in BaSnO_{3-x} single crystal (x=0)

To understand the results, a theoretical calculation in BaSnO_{3-x} assuming a lower symmetry group will be helpful. It will provide a clue in assigning the Raman peaks to a certain vibration mode. Lastly, the annealing appears to reconstruct the surface structure to as it is before polishing. Except the small peak observed at 861 cm^{-1} the Raman spectrum has completely recovered its original spectrum.

While the $x=0$ single crystals were vulnerable to polishing, the crystals that were grown under sufficient oxygen environment did not show any structure distortion under polishing. In summary, the low resistivity BaSnO_3 single crystals which showed strong first order Raman peaks were easily distorted to a lower symmetry structure by polishing while the high resistivity BaSnO_3 which is thought to be an ideal cubic perovskite was more robust under polishing.

From the previous results, we can speculate that the presence of oxygen vacancy caused the low resistivity and the observation of first order Raman peaks which are thought to originate by distortion in the crystal. Therefore, it is worthy to make an attempt to induce oxygen vacancy in the BaSnO_3 single crystals which were grown with the presence of KClO_4 . First, a $x=2$ BaSnO_3 single crystal was annealed at $1000\text{ }^\circ\text{C}$ in Ar gas for one week. However, one week of annealing did not affect the Raman spectrum as show in Figure 4-13.

Thus, a more effective oxygen remover, forming gas (a mixture of 95% nitrogen gas and 5% hydrogen gas), was used. Under forming gas, the single crystal was annealed at $1000\text{ }^\circ\text{C}$ for 100 hours. As a result, the single crystal changed color as in Figure 4-13 (a). The originally yellow smooth surface of the single crystal turned in to a gray color rough surface. When the crystal was cut in half, a shining cleaved surface was shown inside the gray shell. It

appears that the forming gas has completely removed oxygen from the surface leaving a gray shell surrounding the single crystal. Even the single crystal inside has changed color in to dark brown which indicates that oxygen may have been reduced even in the core single crystal. The Raman spectroscopy was taken on this cleaved surface.

Figure 4-13 (b) shows that forming gas has distorted the BaSnO_3 single crystal. Interestingly, the overall Raman spectrum looks similar to the case of $x=0$ $\text{BaSnO}_{3-\delta}$ single crystals after being polished. From the spectra of the two cases, it appears that their structure symmetry have been lowered to a similar space group. The strong peaks at 108, 138, and 250 cm^{-1} exactly coincides with the peaks appeared in the polished $x=0$ single crystal. Also, the set of Raman bands near 380 cm^{-1} and a band between 640 and 710 cm^{-1} are noticeable. However, the peak positions are slightly different compared to the case of the polished $x=0$ single crystal which may be due to the difference in oxygen vacancy density within the crystal causing the bond strength to be different.

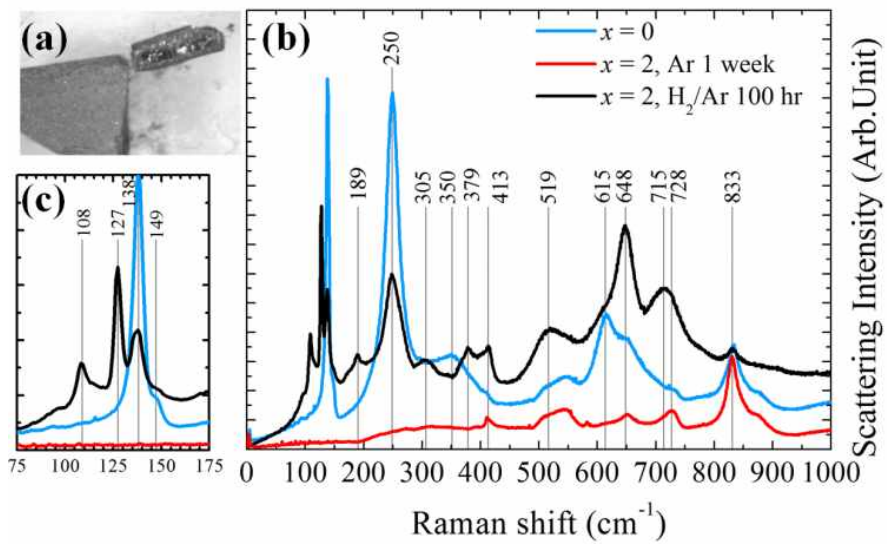


Figure 4-13 Forming gas (H₂/Ar) annealing effect on BaSnO₃ single crystal ($x=2$)

4.4.3 Doped BaSnO₃ single crystals

Previously, our research group succeeded in growing doped BaSnO₃ single crystals in addition to the undoped single crystals. Single crystals were grown by doping La into Ba site and by doping Sb into Sn site. Both cases result in an *n*-type transparent oxide semiconductor. Thorough studies such as structural, electrical, optical, and thermal properties on doped BaSnO₃ single crystals were conducted by Kim *et al* [2, 3]. In addition to the previous results, Raman spectroscopy was taken in the doped single crystals.

The doped single crystals used for Raman spectroscopy were grown without the presence of KClO₄ during flux growth. Therefore, there is high possibility that there are oxygen vacancies in the crystals. The Raman spectroscopy results are represented in Figure 4-14. The overall spectra are similar to the oxygen deficient undoped BaSnO₃ single crystal. A strong first order Raman peak is observed at 138 cm⁻¹. The peak at 250 cm⁻¹ is slightly shifted to 253 cm⁻¹ and became much sharper. Also, the peaks at 350 cm⁻¹ and around 650 cm⁻¹ are present but the absolute Raman shift differs from the undoped crystals. Like the *x*=0 undoped BaSnO₃ single crystal case, the origin of the Raman peaks has not been pinned down. Further studies such as doped BaSnO₃ single crystal growth with the presence of KClO₄ will be an interesting topic. It may give hints on whether the presence of electron carriers causes the anti-bonding states to be occupied and eventually tilting the Sn-O octahedron.

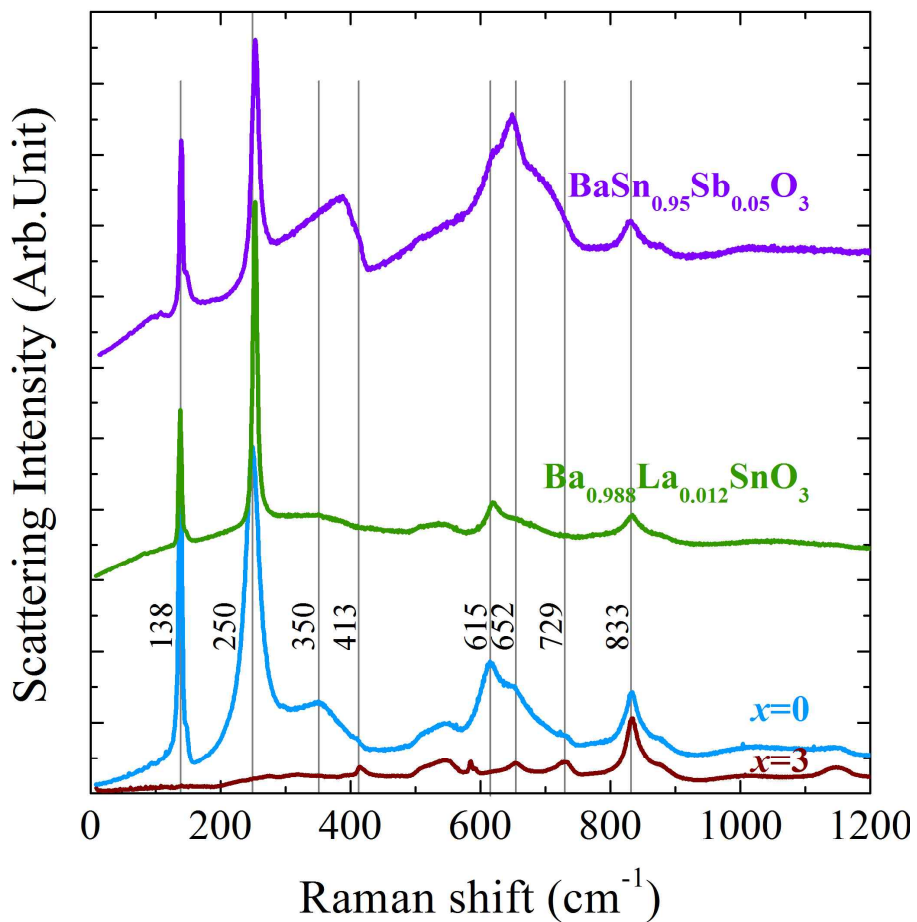


Figure 4-14 Raman spectroscopy on doped BaSnO_3 single crystal in comparison to oxygen vacant ($x=0$) and sufficient ($x=2$) BaSnO_3 single crystal.

Chapter 5

Conclusion

Our group has successfully grown BaSnO₃ single crystals without oxygen vacancy by the addition of KClO₄ during flux growth. Oxidizer is frequently used in high pressure synthesis and pyrotechniques. However, there are not much cases that oxidizer was used in flux growth method. Single crystals were grown in different molar ratio of KClO₄. In terms of color, the grown single crystals can be divided in to two groups; the crystals with less KClO₄ addition ($x=0-1$) showed a blue color while the others grown with sufficient KClO₄ ($x=1.5-3$) showed a yellow color.

The structural properties were investigated through a laboratory x-ray diffractometer. The single crystals appeared to have the same cubic perovskite structure regardless of the amount of KClO₄ added during flux growth. The lattice constants were measured to be $a=b=c=4.117 \text{ \AA}$.

Resistivity verses temperature measurements showed a distinctive behavior between the single crystals. The single crystals that showed a blue color ($x=0-1$) showed a low resistivity less than $\sim 1 \text{ } \Omega\cdot\text{cm}$ while the other group of crystals ($x=1.5-3$) had a high resistivity greater than $\sim 10^{10} \text{ } \Omega\cdot\text{cm}$. The increase in resistivity indicates that the oxygen deficiency has been effectively reduced by the addition of KClO₄.

Optical transmission measurement was done in the range of Mid-IR to UV. The high resistivity samples show a reduction of free carrier absorption which once again supports the idea that the oxygen vacancy has been reduced by the oxidizer. Additionally, the optical band gap reduced slightly as the

oxygen vacancy has been reduced. The reduced optical band gap may indicate the intrinsic direct band gap of undoped BaSnO₃ single crystal while the original greater optical band gap in $x=0$ crystals may be due to Burstein-Moss shift.

Lastly, Raman spectroscopy was taken for the BaSnO₃ single crystals. Even though the x-ray diffraction results did not show any difference between the crystals, Raman spectroscopy results showed different spectra between low resistivity crystals and the high resistivity crystals. The low resistivity crystals showed strong first order Raman peaks while the high resistivity crystals did not. This indicates that the low resistivity crystals may have local distortion while the high resistivity crystals are ideally cubic. We suggest that when electron carriers are present in the crystal they will fill anti-bonding states causing the Sn-O octahedron to tilt. This distortion results in the observation of first order Raman peaks. Additionally, we observed that polishing and forming gas annealing in high resistivity crystals ($x=1.5-3$) causes the first order Raman peaks to emerge.

Reference

- [1] H. J. Kim, U. Kim, H. M. Kim, T. H. Kim, H. S. Mun, B. G. Jeon, K. T. Hong, W. J. Lee, C. Ju, K. H. Kim, and K. Char, *Appl. Phys. Express* **5**, 061102 (2012).
- [2] H. J. Kim, U. Kim, T. H. Kim, J. Kim, H. M. Kim, B. G. Jeon, W. J. Lee, H. S. Mun, K. T. Hong, J. Yu, K. Char, and K. H. Kim, *Phys. Rev. B* **86**, 165205 (2012).
- [3] H. J. Kim, J. Kim, J., T. H. Kim, W. J. Lee, B. G. Jeon, J. Y. Park, W. S. Choi, D. W. Jeong, S. H. Lee, J. Yu, T. W. Noh, and K. H. Kim, *Phys. Rev. B* **88**, 125204 (2013).
- [4] H. Toyosaki, M. Kawasaki, and Y. Tokura, *Appl. Phys. Lett.* **93**, 132109 (2008).
- [5] Q. Liu, J. Liu, B. Li, H. Li, G. Zhu, K. Dai, Z. Liu, P. Zhang, and J. Dai, *Appl. Phys. Lett.* **101**, 241901 (2012).
- [6] H. Mun, U. Kim, H. M. Kim, C. Park, T. H. Kim, H. J. Kim, K. H. Kim, and K. Char, *Appl. Phys. Lett.* **102**, 252105 (2013).
- [7] D. Seo, K. Yu, Y. J. Chang, E. Sohn, K. H. Kim, and E. J. Choi, *Appl Phys. Lett.* **104**, 022102 (2014).
- [8] T. Hahn, *International Tables for Crystallography: Volume A. Space-Group Symmetry* (Springer, Dordrecht, 2005).
- [9] N. W. Ashcrof and N. D. Mermin, *Solid State Physics* (Brooks/Cole, Belmont, 1976) p.10.
- [10] M. Fox, *Optical Properties of Solids* (Oxford, New York, 2010).
- [11] J. R. Ferraro, K. Nakamoto, and C. W. Brown, *Introductory Raman Spectroscopy* (Academic press, San Diego, 2003).
- [12] P. J. Larkin, *IR and Raman Spectroscopy: Principles and Spectral Interpretation* (Elsevier, Waltham, 2011).
- [13] H. Kuzmany, *Solid-State Spectroscopy: An Introduction* (Springer, Heidelberg, 2009).
- [14] M. I. Aroyo, J. M. Perez-Mato, D. Orobengoa, E. Tasci, G. de la Flor, and A. Kirov, *Bulg. Chem. Commun.* **43**, 183 (2011)
- [15] D. A. Long, *Raman Spectroscopy* (McGraw-Hill, London, 1977)

- [16] B. Okai, Jpn. J. Appl. Phys. **28**, L2251 (1989).
- [17] B. Okai, Jpn. J. Appl. Phys. **29**, L2180 (1990).
- [18] B. Okai, Jpn. J. Appl. Phys. **30**, L179 (1991).
- [19] P. Laffez, X. J. Wu, S. Adachi, H. Yamauchi, and N. Mori, Physica C **222**, 303 (1994).
- [20] X. Kang, J. Zhang, Q. Zhang, K. Du, and Y. Tang, J. Therm. Anal. Calorim. **109**, 1333 (2012).
- [21] N. F. Mott, *Metal–Insulator–Transition*, Taylor and Francis, London (1990).
- [22] E. Moreira, J. M. Henriques, D. L. Azevedo, E. W. S. Caetano, V. N. Freire, and E. L. Albuquerque, J. Solid State Chem. **187**, 186–194 (2012).
- [23] H. R. Liu, J. H. Yang, H. J. Xiang, X. G. Gong, and S. H. Wei, Appl. Phys. Lett. **102**, 112109 (2013).
- [24] B. G. Kim, J. Y. Jo, and S. W. Cheong, J. Solid State Chem. **197**, 134–138 (2013).
- [25] S. Sallis, D. O. Scanlon, S. C. Chae, N. F. Quackenbush, D. A. Fischer, J. C. Woicik, J. H. Guo, S. W. Cheong, and L. F. J. Piper, Appl. Phys. Lett. **103**, 042105 (2013).
- [26] D. O. Scanlon, Phys. Rev. B **87**, 16201(R) (2013).
- [27] D. Seo, K. Yu, Y. J. Chang, E. Sohn, K. H. Kim, and E. J. Choi, Appl. Phys. Lett. **104**, 022102 (2014).
- [28] K. S. Aleksandrov, Ferroelectrics **14**, 801 (1976).
- [29] N. W. Thomas, Acta Cryst. **B54**, 585 (1998).
- [30] E. Moreira, J. M. Henriques, D. L. Azevedo, E. W. S. Caetano, V. N. Freire, and E. L. Albuquerque, J. Solid State Chem. **184**, 921 (2011).

국문 초록

투명 전도체 산화물은 디스플레이, 광기전력 발전 그리고 고효율 유리창 등 산업적으로 유용성이 높아 연구가 많이 되었다. 특히, 인듐주석산화물, 불소 함유 주석산화물 그리고 알루미늄 함유 아연산화물이 산업에서 많이 사용되고 있는 물질이다. 하지만 이러한 물질들도 가격경쟁력 및 산소 안정성 등에 있어서 개선의 여지가 남아있다. 본 연구실에서는 이러한 문제점이 적은 바륨 주석 산화물 단결정을 성장하여 보고한 바가 있다. 특히, 란타늄 혹은 안티모니를 함유한 바륨주석산화물의 경우에 대한 연구가 되었으며 그 중에 란타늄 첨가시 전자 이동도가 $320 \text{ cm}^2\text{V}^{-1}\text{s}^{-1}$ 으로 타 투명 전도체 산화물과 비등하거나 높았다. 하지만, 박막에서는 전자 이동도가 $70 \text{ cm}^2\text{V}^{-1}\text{s}^{-1}$ 으로 단결정의 그것보다 낮게 나타났으며 이는 기판과 박막의 격자 상수의 차이에 의한 것이라는 보고가 있었다. 따라서, 도핑이 되지 않은 바륨주석산화물을 기판으로 사용하여 격자 상수에 의한 차이를 없애고자 했으나 도핑 되지 않은 단결정에서는 산소 빈자리에 의해 $\sim 10^{18} \text{ cm}^{-3}$ 의 전자 운반자 농도가 존재하여 기판으로 사용이 어려웠다.

본 연구실에서는 산화제인 KClO_4 를 플럭스에 첨가하여 산소 빈자리가 없는 단결정을 성장하였다. 이 논문에서는 KClO_4 의 몰비율을 다르게 하여 성장한 단결정의 여러 물리적 성질을 비교하여 연구하였다. 엑스선 회절 분석 결과 산화제의 몰비율에 무관하게 동일한 입방 페로브스카이트 구조로 격자상수가 동일하게 $a=b=c=4.117 \text{ \AA}$ 으로 측정되었다. 산화제의 첨가량이 증가함에

따라 전기저항이 $\sim 10^{-3} \Omega\cdot\text{cm}$ 에서부터 $\sim 10^{11} \Omega\cdot\text{cm}$ 까지 변화였다. 전기 저항이 작은 단결정 군과 큰 단결정 군으로 나뉘었으며 전기 저항이 작은 경우 푸른색이었으며 전기 저항이 큰 경우 노란색을 띠었다. 투과 실험을 중간 적외선부터 자외선까지 실행한 결과 전기 저항이 큰 단결정 군에서 자유 전자에 의한 흡수가 현저히 줄어든 것을 확인하였다. 엑스선 회절 무늬가 단결정의 온곳 대칭성에 대해 민감하다면 라만 분광법을 통해서도 국소 대칭성을 확인할 수 있다. 라만 분광법을 통해 단결정을 측정된 결과 전기 저항이 큰 단결정 군과 작은 단결정 군의 스펙트럼이 다르게 나타났다. 전기 저항이 작은 단결정 군에서 일차 라만 진동 모드에 의한 봉우리가 강하게 나타나 국소적으로 찌그러짐이 있음을 시사했다. 반면 전기 저항이 큰 단결정에서는 일차 라만 진동 모드가 발견되지 않아 이상적인 입방 구조를 가지고 있음을 나타냈다. 편광 라만법을 이용하여 일차 라만 진동 모드를 정의하고자 했다. 또한, 연마와 열풀림이 바륨주석산화물 단결정에 미치는 효과도 라만 분광법을 통해 확인했다.

주요어: 투명 전도체 산화물, BaSnO_3 , 입방 페로브스카이트 구조,
라만 분광법

학 번: 2012-20366